Electrochemical Characteristics of DNA Modified Electrode as a Function of Coverage

Rahul Tevatia,[a] Abhijeet Prasad,[b] Ravi F. Saraf*[b]

[a] Vajra Instruments, Lincoln, NE 68512; [b] Department of Chemical and Biomolecular Engineering, University of Nebraska-Lincoln, NE 68512; *rsaraf2@unl.edu

Electrochemical Characteristics of DNA Modified Electrode as a Function of Coverage

Rahul Tevatia,[a] Abhijeet Prasad,[b] Ravi F. Saraf*[b]

[a] Vajra Instruments, Lincoln, NE 68512; [b] Department of Chemical and Biomolecular Engineering, University of Nebraska-Lincoln, NE 68512; *rsaraf2@unl.edu

ABSTRACT: Electrochemical characteristics of immobilized dsDNA on Au electrode was studied as a function of coverage using a home-built optoelectrochemical method. The method allows probing of local redox processes on a 6-μm spot by measuring both differential reflectivity (SEED-R) and interferometry (SEED-I). The former is sensitive to redox ions that tend to adsorb to the electrode while SEED-I is sensitive to nonadsorbing ions. The redox reaction maxima, R_{max} and Δ_{max} from SEED-R and SEED-I, respectively, are linearly proportional to amperometric peak current, I_{max}. The DNA binding is measured by a redox active dye, methylene blue (MB), that intercalates in dsDNA leading to an R_{max}. Concomitantly, the absence of Δ_{max} for $[Fe(CN)_6]^{4-/3-}$ by SEED-I ensures that there is no leakage-current from voids/defects in the alkane thiol passivation layer, at the same spot of measurement. The binding was regulated electrochemically to obtain the binding fraction, f, ranging about three orders of magnitude. A remarkably sharp transition, $f = f_T = 1.25 \times 10^{-3}$ was observed. Below f_T, dsDNA molecules behaved as individual single-molecule nanoelectrodes. Above the crossover transition, R_{max}, per dsDNA molecule dropped rapidly as $f^{-1/2}$ towards a planarlike monolayer. The SEED-R peak at f ~3.3 x 10^{-4} (~270 dsDNA molecules), was (statistically) robust corresponding to a responsivity of ~0.45 zeptomoles of dsDNA/spot. Differential pulse voltammetry (DPV) in the single-molecule regime estimated that the current per dsDNA molecule was ~4.1 fA. Comparing with published amperometric results, the reported semi-logarithmic dependence on target concentration is in f > f_T regime.

Introduction

A DNA monolayer immobilized on Au electrode by a gold-sulfur (Au-S) linkage is of great scientific and technological interest as a model organic monolayer, and for use in biosensing.[1-5] Easy immobilization of single-stranded DNA (ssDNA) by a Au-S linkage[5] and the electronic conductive property of double-stranded DNA (dsDNA)[6] led to the development of compact, inexpensive, electrochemical sensors and devices. A large change in the refractive index due to conductivity in dsDNA[7] is leveraged to make sensitive surface plasmon resonance devices on nanostructures of Au.[8-10] Recently, the insulator-conductor transition has become an attractive principle for developing high-impact liquid biopsy applications for detection of cancer by profiling cell-free nucleic acids (cfNA).[11,12]

The importance of electronic conduction in dsDNA for electrochemical devices was realized at the onset as the charge injection was accomplished via redox coupling.[13,14] The conduction is attributed to overlapping of π orbitals in the base pairs[13,15] leading to short range transport by nonresonant tunneling[16] and long-range conduction by hopping between adjacent bases.[15,17] The long-range conduction in the relatively hydrophobic core surrounded by (electronically insulating) an ionic polyelectrolyte shell in water,[17] is a unique prescription for building electrochemical devices by intercalation mediated charge injection to gate conduction,[15] couple reactions,[6] measure disruptions in the stacking to probe single-base mutation[18] and heavy ions,[19] and using redox active intercalator compounds to measure specific binding between an immobilized ssDNA probe and an ssDNA target.[6,20] Using redox active reporters, sensitivity in the attomolar range has been demonstrated.[21] The high sensitivity and dynamic range of these label-free methods will lead to technology to profile cfNA without using polymerase chain reaction (PCR).

The binding of the target to an immobilized probe is affected by electrostatic effects, namely: (i) the probe sticks to the Au surface, and (ii) the negative charge on the probe and target causes repulsion. First, as Au has propensity to attract anions due to its lower Fermi level,[22] the negatively charged ssDNA probe will tend to lie flat on the Au electrode due to strong electrostatic attraction. The flattening of tethered DNA on Au is shown directly by neutron reflectivity.[23] The strong electrostatic interaction greatly inhibits the binding that may be enhanced by backfilling the electrode with alkane thiols, such as mercaptohexanols (MCH).[24] The "lifting" of the immobilized ssDNA from the Au electrode due to MCH backfilling is directly shown by fluorescence[25] and neutron reflectivity.[23] Applying negative potential to the electrode lifts the tethered ssDNA probe,[26,27] which partly explains the significant enhancement in binding on application of periodic electrochemical potential.[12,28,29] Second, several studies have clearly demonstrated that electrostatic repulsion tends to reduce binding as the target as the probe coverage increases.[30-33] For example, measurement of surface charge by electrochemical impedance spectroscopy (EIS) indicates that DNA charge is not completely

screened by the ions in the solution to cause electrostatic repulsion that limits binding at high probe coverage.[30,31] Surface Plasmon Resonance (SPR) studies probing binding in real-time indicate that both kinetics and percent binding depend on the probe converge.[34] Studies controlling the probe density shows the optimum coverage of the probe to obtain efficient binding is in 2.5×10^{12} to 4.5×10^{12} ssDNA/cm^2 range with,[31,35,36] or without MCH backfill.[34] In an interesting study, interprobe distance was fine-tuned using a DNA origami scaffold to show that an optimal distance for efficient binding to achieve sensitivity of 1 fM was ~9 nm,[37] equivalent to a coverage of ~1.6×10^{12} ssDNA/cm^2.

While careful studies on the chemistry of ssDNA immobilization and its effect on percent binding have been reported, surprisingly, little is understood about responsivity, i.e., explicit effect of current per molecular binding as percent binding increases at fixed (optimum) probe coverage. The responsivity is directly related to the sensitivity, and target quantification that is determined by change in electrochemical signal as a function of percent binding at fixed probe coverage. It is expected that, at low binding fraction with a large interduplex distance, d_T, each molecule will contribute individually to the redox current (Fig. 1(a)) where, the current per molecule will be constant, independent of ensemble size, i.e., ergodic. The current rise will be proportional to the binding number fraction, i.e., colligative. However, as the fraction of binding increases the diffusion domains, δ, will begin to overlap leading to lower current per molecule (Fig. 1(a)), i.e., nonergodic and non-colligative. (The size of diffusion domain, δ, at a fixed potential scan rate, redox-ion concentration, and ion diffusivity[37] will typically be constant during a readout process.) Considering each dsDNA molecule as a nanoelectrode, the transition from individual to overlap regime should occur at $d_T \sim 6L_P$, where L_P is the effective (average) radius of the nanoelectrode.[38-40] In this study, we attempt to locate the transition, and (importantly) determining if this transition occurs in the range of reported DNA array studies to measure [c]. A surprisingly sharp transition in DNA electrode characteristics was observed from the "single molecule regime" (i.e., ergodic, Fig. 1(a)) to the "planar electrode regime" (i.e., nonergodic, Fig. 1(b)). The single molecule regime with colligative response could open DNA chip applications, such as using them as bionanowires to interconnect individual proteins to underlying electrodes.

To study the effect of percent binding at fixed (optimum) probe coverage, the overlap of diffusion domains of redox species between the dsDNA sites needs to be deconvoluted to determine redox per dsDNA molecule. High sensitivity at low percent binding is required with (direct) determination of percent binding and probe coverage. Furthermore, no redox background from pinholes in the passivation layer should contribute to the overall signal, especially at low percent binding where the signal will be low. To ensure no background, we locally measure redox by averaging over several (~6 μm diameter) spots by differential interferometry and reflectivity. The interferometry measurement ensures no background from the pinholes at the same spot where the redox from dsDNA is measured by reflectivity.

Similar to SPR based optical reflectivity methods to measure local redox;[41-43] the studied optical method also relies on modulation in the interfacial refractive index during redox. Here, the charge modulation at the interface during redox is directly measured by applying a small AC potential to produce a differential reflectivity and interferometry signals that are concomitantly probed to obtain at least three orders of magnitude better sensitivity than cyclic voltammetry. From differential reflectivity sensitivity, the method is over two orders more sensitive than SPR approach.[41,43]

Experimental

Materials. All the chemicals used in the study are from commercial sources (Supporting Information (SI), Section S1). Ultrapure DNase/RNase free distilled water (Invitrogen®) was used to make all stock and buffer solutions. Two types of synthetic probes and one synthetic target were used (SI, Section S1). The ~22 nucleotide long synthetic probes of sequence complimentary to miRNA 155 and 21, respectively have a –(CH$_2$)$_6$-SH linker at the 5'-end. The target is synthetic miR-155.

DNA Chip Fabrication. A 1 cm^2 Silicon chip (SiO$_2$/Si) with five 0.8 x 8 mm and two 0.8 x 6 mm (control) Au electrodes were patterned by standard lithography (SI, Fig. S1). There were four steps to make the DNA electrode in an array of seventy-two 50 μm diameter microwells (see SI, Section S2, Fig. S2-S4 for details, and prior publication[12]). The binding in step 3, was performed electrochemically (SI, Fig. S4). The chip was vigorously washed between each step by dipping the sample for about 120 s in 50 mL beaker with DNase/RNase-free water stirred at ~700 RPM.

Characterization: Probe Coverage (N_P), Binding Coverage (N_T), and Binding Fraction ($f = N_T/N_P$). All the 72 microwells on each of the five electrodes of the chip were immobilized with P155 probes. Different electrochemical redox binding (EREB) condition was applied on each electrode with fresh solution. The difference in miR-155 target copy number in 500-μL solution of EREB before and after binding was measured by qPCR (QuantStudio™ 3 Real Time PCR, Applied Biosystems) to obtain target molecule coverage, N_T. The details of the qPCR method and the standard curve are described in SI, Section S3.

Subsequently, the Au-S linkage was electrochemically cleaved by applying a CV ramp from -1.0 V to +0.5 V in 50 mM K$_4$[Fe(CN)$_6$]. The solution was analyzed by qPCR to obtain the copy number of the cleaved probe (N_P). From the binding fraction, $f = N_T/N_P$, as a function of EREB conditions was obtained for each electrode. The N_P was also measured by fluorescence (SI, Section S6).

Probe-Target Binding Readout by Local Redox. The probe-target binding was measured in a solution of 10 μM MB and 50 mM K$_4$[Fe(CN)$_6$] in 100 mM PB (pH 7.6). The (blue) MB$^+$ specifically binds to dsDNA and reduces to (colorless) leucomethylene blue (LMB).[12,20] The redox was measured locally on a 6-μm spot defined by the He-Ne laser beam by an electrochemical-optical method.

Data quality. For an acceptable data set, the control electrodes must satisfy the following conditions. (i) The redox signal on microwells with P155 and P21 probes (with no

EREB) must be zero. No redox signal from ssDNA probes (P155 and P21) indicates that the redox signal (on active electrode) was exclusively from dsDNA. (ii) No redox signal from the blank microwell should be observed. This confirmed that the MCH backfilling process was complete. An important aspect (as discussed in Fig. 5) was to also confirm zero background on the spot where specific binding is measured. Well over 10 and 3 spots per active and control electrode were measured to yield statistically robust data that was absolute with zero background for different EREB conditions. The redox signal for each spot was averaged over at least 10 CV cycles.

The Electrochemical-Optical Readout

The underlining principle for measuring local redox is to probe the (relative) change in the ionic charge at the solution/electrode interface as the applied potential, E, between the electrode and solution (i.e., reference electrode) is varied during CV. The charge is measured by the refractive index modulations.[44] At equilibrium and quasi-equilibrium states, the field emanating from the electrode is screened by the electrical double-layer (EDL). However, close to the redox potential, the faster exchange of electrons between redox ions and the electrode compared to the slower diffusion of (compensating) ions, the EDL will be significantly discharged causing the field to penetrate deeper.[45-47] The modulation in descreening of the field is measured by superimposing a small AC potential at a frequency of ω on the CV cycle. Typically, the amplitude and frequency of the AC potential is 10^{-1} and 10^3 fold of the CV potential, respectively. To ensure that the AC potential does not significantly perturb the electrochemistry during CV, the amplitude of the AC potential is small enough to maintain linearity of the system, i.e., second order effects (at 2ω) are less than 1% of the signal at ω. As the redox current increases, the ion oscillations at ω will increase due to the discharge of the EDL. Thus, by measuring the amplitude of oscillation of ions at the AC potential frequency, ω, it is possible to quantitatively measure the local redox current. As the beam can scan over the electrode, the instrument is called Scanning Electrometer for Electrical Double-layer (SEED). Both differential reflectivity (SEED-R) and differential interference (SEED-I) are measured by SEED during CV. The SEED-R that probes ion concentration modulation close to the electrode surface is more sensitive to redox of ions that tend to adsorb to the electrode surface. The SEED-I measures change in optical path length due to ion concentration penetrating significantly deeper in the diffuse EDL.

The principle for simultaneous measurement of differential interferometry and reflectivity is derived and discussed in detail in SI, Section S4. Briefly, the polarized beam is split into two orthogonally polarized beams sample and reference beams, of equal intensity using a calcite crystal (CXL) (Fig. 2). The reference beam was incident on the passivated electrode, while the sample beam falls on the electrode subjected to AC potential. The AC amplitude of 100 mV is small enough that the system is linear. The reflected (sample) beam with oscillating reflectivity of amplitude R_o (SI, Eq. (9) and (10a)) and oscillating (interference) phase of amplitude, ϕ (SI Eq. (3) and (4)) with respect to the reference

beam, are superimposed in the CXL to form a polarized light where the polarization direction is oscillating at ω. The light from the CXL is split again into two orthogonally polarized lights by a Wollaston prism (Fig. 2). For the polarization of the Wollaston at 45^0 with respect to the CXL, the AC and DC intensities are measured on the detectors A and B (Eq. (12) in SI). By electronically subtracting and adding the two signal, A and B at the respective detectors (Eq. (13), SI), normalizing with respect to the total laser intensity, $(A + B)_{DC}$, and nulling the $(A – B)_{AC}$ signal (see "The Nulling", SI, Section S4); both the Δ and R are obtained concomitantly in real time during CV cycle as (also see, Eq. (15) and (16) in SI),

$$\left|\frac{(A-B)_{AC}}{(A+B)_{DC}}\right| = \Delta = \frac{4\pi}{\lambda}z_o + \frac{4}{k_2}\delta n_s \text{ (SEED-I raw signal)} \quad (1)$$

$$\left|\frac{(A+B)_{AC}}{(A+B)_{DC}}\right| = R = 2K_1\delta n_s \quad \text{(SEED-R raw signal)} \quad (2)$$

The AC signals are the (small) oscillation in the laser intensity riding over the total laser intensity, $(A + B)_{DC}$. The $(A - B)_{AC}$ signal is the amplitude of oscillation in the intensity of the light due to the interference between the reference and sample beam. The $(A + B)_{AC}$ is the amplitude of oscillation in the intensity of reflected sample beam due to AC potential. The parameters in Eq. (1) and (2) are as follows: The amplitude of the path length oscillation due to the AC potential, z_o is given by, $z_o \approx (dn_-/dc)\kappa<\delta c_->$, where (dn_-/dc) is the differential refractive index of the anions, κ is the penetration depth of the AC electric filed, and $<\delta c_->$ is amplitude of oscillation of anion concentration averaged over κ (see Eqs. (2) and (3) in SI). The refractive index oscillation due to AC potential at the interface is $\delta n_S \approx (dn_-/dc)<\delta c_S>$, where $<\delta c_S>$ is amplitude of oscillation of the anion concentration at the surface due to AC potential (see Eq. (10a) in SI). The constants, k_2 is complex refractive index of the electrode, and K_1 is defined in Eq. (10a) of SI.

R is exclusively due to near-electrode modulation, δn_s (defined in SI, Eq. (9)) while the former is a combination of near-surface and far-surface effects (i.e., z_o, defined in SI, Eq. (3)). An aspect worth mentioning about the optics is that the interference occurs in CXL (rather than air); and the R and S beams are close, about 100 μm apart, thus the drift and differential thermal noise is very low.

Results and Discussion

The Nature of the SEED Signal. For all of the SEED studies, the amplitude and frequency, ω, of AC potential was 100 mV and 2 KHz, respectively. The potential ramp rate for CV was 500 mV/s which corresponded to an effective frequency of ~0.36 Hz. To demonstrate the SEED-I and R modes, we considered two simple redox ions: $K_4[Fe(CN)_6]$ and MB, respectively. Fig. 3(a) shows a typical SEED-I raw data, Δ for 50 mM $K_4[Fe(CN)_6]$ in 100 mM PB over ten CV scans signal with low noise. We superimposed each scan to obtain the average signal, $<\Delta>$ and $<R>$ as a function of E. The error halo was due to deviations among the scans (Fig. 3(b)). For the same CV scan, while SEED-I signal, $<\Delta>$, showed a strong oxidation and reduction peaks, SEED-R signal, $<R>$, exhibited no redox peak (Fig. 3(b)). Based on Eq. (1) and (2), the oscillation near the surface, δn_s, was insignificant compared to the cumulative, long-range oscillation of the ions, z_o (as defined in Eq. (3), SI). The z_o was enhanced around the redox

due to a larger penetration distance of the electric field, κ (defined in Eq. (3), SI), leading to signal amplification. Thus, the "near surface" effects were insignificant compared to "far surface" effects for conventional turnover electrochemical reaction at the electrode. The inference is reasonable because $[Fe(CN)_6]^{4-/3-}$ does not adsorb to Au electrode.

We note in passing that although the absolute amplitude of oscillation, $<\Delta>\lambda/4\pi$, of about $\sim$2.5 picometers was well below the diffraction limit, it does not break the diffraction limit because we are measuring differential signal. Furthermore, consistent with previous study,[46] Δ_{max} and I_{max} measured concomitantly during CV showed (as expected) a linear relationship (Fig. 3(c)). Although the signal-to-noise ratio for CV and SEED-I are comparable (SI, Fig. S7), the peak for the latter was much more well defined; and the area is over three orders of magnitude smaller.

The nature of the response for MB is different (Fig. 3(d)). Both R and Δ were observed, implying that both z_o and δn_s are significant. However, as MB tends to adsorb on the Au electrode,[48] the SEED-R mode signal is significantly large. As R had low noise; and it is only dependent on δn_s (see Eq. (2)); to measure DNA binding by MB that binds to dsDNA, SEED-R will be the primary signal. Importantly, we note that two beams are not required for SEED-R. By clipping one of the two beams exiting from the CXL and accounting for the 50% decrease in the incident intensity, i.e., $(A + B)_{DC}$, the SEED-R signal from one versus two beams is virtually unchanged, indirectly substantiating the quantitative nature of the optics (SI, Fig. S8).

The Signals from the Electrochemical Chip: Specific Binding and Controls. After the probe spotting, EREB, and MCH backfilling, a typical SEED-R signal on a P155 spot that specifically binds to the target miR155 showed oxidation and reduction peaks of MB^+/LMB that was stable over several CV cycles (Fig. 4(a)). The small error halo indicated good cycle-to-cycle repeatability (Fig. 4(b). On the same chip, the typical response for the controls showed the following: First, the signal on the blank on the control electrode showed no signal indicating that MCH passivated the electrode, thus, the background from MB redox was unmeasurable. Second, the signal from ssDNA (for both P155 and P21) did not exhibit any redox peak, implying that the signal of binding was exclusively from dsDNA (i.e., the signal was absolute). In other words, measured redox is exclusively via transport of electron through the π-π stacking of base pairs in the core of the double helix.[45] For reliable data, all of the controls were (strictly) satisfied (Fig. 4(b)).

The readout for percent binding is defined by the reduction peak, i.e., $MB^+ + e^- \rightarrow LMB$. The baseline due to signal from ubiquitous oscillations of the buffer ion at the interface due to the AC potential is subtracted to obtain R_{max}. Consistent with a previous study on SEED-R with a single beam,[16] R_{max} had logarithmic dependence on [c] for N_{CV} = 16 cycles (Fig. 4(c)). Five concentrations were measured per chip. The error-bar was based on $\sim$10 points/electrode for a given [c]. The semi-log behavior, similar to conventional redox measurements,[15,46,47] further supports the linear correspondence between I_{max} and R_{max}. The SEED-R for heavy metal redox is also linearly proportional to I_{max} obtained by CV.[48]

Importance of Zero Background: MCH Backfilling. To obtain reliable data over a large range of f, blocking redox from the voids in the MCH passivation layer is critical. We compared characteristics from two chips at N_{CV} = 32 cycles, [c] = 1 fM, with incomplete and complete backfilling of the MCH passivation, respectively. For incomplete backfilling, the second step of incubation was not performed. In SEED-I, the redox peak for $[Fe(CN)_6]^{4-/3-}$ was observed on the blank microwell of control electrode which was lower than base electrode indicating (only) partial passivation (Fig. 5(a)). No $[Fe(CN)_6]^{4-/3-}$ redox was observed for complete backfilled chip (Fig. 5(a)) indicating void-free passivation. Also, the MB^+/LMB redox for the blank microwell on control electrode, the incomplete backfilled chip showed a peak while the complete backfilled chip had no redox signal (Fig. 5(b)). Remarkably, Consistent with the reported absorption of MB to Au,[52] after exposing the incomplete backfilled chip to 10 μM of MB for 30 min followed by vigorous washing, the redox of MB^+/LMB persisted in solution without MB (Fig. 5(b)). Thus, the observation in Fig. 3(d) supports Eq. 2. (The incomplete passivation led to a redox peak for MB in all of the microwells (SI, Fig. S10).

The (serious) consequence of background redox from incomplete MCH passivation for quantification is realized by comparing the signals on the active microwell (Fig. 5(c)). The redox peak for $[Fe(CN)_6]^{4-/3-}$ measured by SEED-I for the incomplete backfilled chip was comparable to the blank microwell (in Fig. 5(a)), while no peak was observed for the complete backfilled chip. However, due to the voids in the incomplete backfilled chip, the corresponding MB redox by SEED-R on the same spot was significantly enhanced compared to the completely backfilled chip (Fig. 5(c)). From the calibration curve[12] (SI, Fig. S11), the estimated [c] for the complete and incomplete backfilled chips with R_{max} of $\sim$10^{-4} and $\sim$4x10^{-4}, respectively, was $\sim$1 fM and $\sim$10^3 fM. The 10^3 fold error in [c] due to the background is significant. A similar sensitivity to background on error would be obtained by measuring the current because the peak current is proportional to log[c]. Therefore, elimination of the background due to backfilling is critical.

Regulating Binding Fraction (f) by EREB. EREB was performed in a 500-μL solution. As the CV potential was positive, the negatively charged ssDNA targets were attracted toward the electrode. As the potential was beyond +220 mV, $[Fe(CN)_6]^{4-}$ oxidized to $[Fe(CN)_6]^{3-}$ causing the EDL to discharge, similar to the principle of SEED. As a consequence, the electric field penetration depth significantly enhanced to sequester target ssDNA from depths beyond EDL thickness of $\sim$10^2 nm to diffusion thickness of typically 10^0 μm.[53] As a result, due to the oxidation of $[Fe(CN)_6]^{4-}$ more ssDNA targets from 100-fold larger distances were attracted toward the electrode. The increase in R_{max} for specific binding by adding $[Fe(CN)^6]^{4-}$ during EREB was by $\sim$10^{-4} (SI, Fig. S12). From the calibration curve (SI, Fig. S11), the rise by $\sim$10^{-4} was an equivalent increase in [c] by well over two orders of magnitude. Based on the binding kinetics map (SI, Fig. S13), we chose the following EREB conditions to cover the (largest) possible range of f: (i) for high f regime, N_{CV} was constant at 32, while [c] was varied from 10^2 to 10^3 fM; (ii)

for low f regime, [c] was fixed at 100 fM; and N_{CV} was varied from 2 to 28 cycles.

Master Curve: R_{max} as a Function of Binding Fraction (f). The change in [c] of target molecules before and after EREB was measured by qPCR to determine the copy number of the target molecules binding to the probes for each electrode (see Experimental and SI, Section S2c). The number of target molecules (before binding) in the EREB chamber for [c] = 10^2 to 10^3 fM were 3×10^7 to 3×10^8. The samples were concentrated 100 times using small (<50 nts) DNA/RNA extraction columns (Clontech Lab., Inc). The efficiency of the column was measured to be 63.58% using 100 pM targets. The concentrated solutions had a copy number of 6.02×10^8 to 8.43×10^{10}, well within the linear region of the qPCR calibration curve (SI, Fig. S5). From the difference in copy number, the coverage of target binding, N_T (in molecules/cm^2) was obtained. For the lowest binding fraction, at N_{CV} = 2, a change in Ct value of 0.15 ± 0.001 was measured which was well within the sensitivity in the linear range of the standard curve (SI, Fig. S5).

Subsequently, we measured the N_P on each of the above electrodes. The chip was washed, and the Au-S linkage was electrochemically cleaved by applying a CV ramp from -1.0 V to +0.5 V in 50 mM $K_4[Fe(CN)_6]$. The Au-S linkage is known to cleave due to high negative potential above -0.8 V.[54] As MCH and DNA were removed from the chip exposing the underlying Au, a peak due to redox of $[Fe(CN)_6]^{4-/3-}$ began to appear in differential interferometry (SI, Fig S12). The Δ_{max} monotonically increased to plateau within 5 min (SI, Fig. S15). After 5 min, the redox peak was similar to bare Au (SI, Fig. S16) indicating all of the DNA and MCH molecules were removed. From the qPCR on the cleaved probes, the Ct value of 22.615 ± 0.075 was well within the linear region of the standard curve (SI, Fig. S5) with an estimated copy number of a probe of $3.51 \pm 0.76 \times 10^9$ in 3.75 µl of RT reaction or an estimated coverage of N_P of $2.93 \pm 0.14 \times 10^{12}$ copies/cm^2. The cumulative error bar over 20 chips was remarkably tight. We note in passing that the tight error bar is primarily attributed to the "clean Au electrode" due to O_2-plasma after lithography. The f $(=N_T/N_P)$ was obtained for each chip from the respective N_P and N_T measured by qPCR. The resulting range of f obtained was 3.3×10^{-4} to 1.28×10^{-1} corresponding to an average R_{max} of 3.92×10^{-6} to 2.33×10^{-4} which was well within the measurability of SEED.

To ensure the reliability of the qPCR method, we obtained coverage by fluorescence in an independent experiment (for detailed discussion see SI, Section S6). Briefly, the probes with Cy-3 tag were immobilized on a patterned Au electrode. The peaks were resolved by fitting a Gaussian curve (SI, Fig. S17(a) and Table S1). A calibration curve was obtained by measuring Cy3 fluorescence peak, I_F as a function of known amount of molecules deposited on MCH passivated Au surface of same are area (SI, Fig. S17(d)). From the fluorescence of immobilized probes and the calibration curve, the probe coverage, N_P, was estimated to be $2.9 \pm 0.4 \times 10^{12}$ molecules/cm^2. The error was based on five chips. The coverage measured by fluorescence and qPCR was consistent, indicating that the coverage of probe ssDNA was uniform in the 50-µm microwell.

Discussion on the Master Curve: Single Molecule Electrochemistry. The "universal" behavior of R_{max} versus f that is independent of the binding method exhibited two remarkably clear regimes with a transition at $f_T \sim 1.25 \times 10^{-3}$. Although the transition appeared sharp due to the independent curve fitting in the two regions in Fig. 6(a), it was reasonably broad (Fig. 6(b)), in the magnified view. The broadening may be attributed to local fluctuations in ssDNA and dsDNA number densities.

At f < f_T, R_{max} was linearly proportional to f, indicating the colligative nature of the electrochemical signal where each probe-target molecule is an independent "nano-electrode," i.e., a single-molecule monolayer electrode (SME). In the SME condition, the average signal per molecule, $R_{max}/N \sim 3 \times 10^{-8}$, is independent of the ensemble size, N over a broad measurable range from about 270 to 1000 molecules, i.e. ergodic regime (Fig. 6(a)). At the lowest measured value of f $\sim 3.3 \times 10^{-4}$ (N_{CV} = 2, [c] = 100 fM), R_{max} of 3.9×10^{-6} was well above the baseline with reasonably low variations among various microwells on the same electrode (Fig. 6(c)). From ratio in the sensing area, the corresponding responsivity at the lowest f measured 270 dsDNA molecules or 0.45 zeptomoles was well over two orders of magnitude lower than the reported attomolar sensitivity of amperometric devices.[11,21,49]

The average intermolecular dsDNA spacing, d, at threshold, f_T, was $d_T \sim 80$ nm. Assuming a classical picture (Fig. 1),[38,40] the effective radius of the dsDNA molecular electrode, L_P, was 80/6 $\sim$13 nm. The result may be fortuitous but reasonable: As the dsDNA was well within the persistence length of $\sim$39 nm, the 23 nt dsDNA is a rodlike chain of a contour length of $\sim$13 nm (including the methylene linkage). Thus, the effective radius carved by the tethered dsDNA due to thermal motion will lead to a molecular electrode of radius, $\sim$13 nm.

At f > f_T, the rise in signal was significantly slower, corresponding to $R_{max} \sim f^{0.5}$ which can be explained as follows. As each dsDNA can be considered to be a nanoelectrode, δ is proportional to L_P.[32] Due to the overlap at f > f_T, the diffusion domains will be clipped to $\sim d/\alpha$ (assuming the ions will be partitioned among the α nearest neighbours, where the coordination number, α would be typically between 3-6). As a result, current (per dsDNA electrode) is proportional to d/α. Because R_{max} is linearly proportional to the current, $R_{max}/N \sim d/\alpha$. By geometry, N $\sim$ f and d $\sim N^{-0.5}$, therefore, $R_{max} \sim f^{0.5}$ and $R_{max}/N \sim N^{-0.5}$, consistent with the observation (Fig. 6(a)). Thus, each dsDNA behaves as an individual molecular electrode (or a nanowire) with redox kinetics similar to a classical nanoelectrode disc of radius, $L_P \sim$ the molecular length.

The current from individual dsDNA was estimated by differential pulse voltammetry (DPV) (Section S7, SI). DPV after EREB and MCH backfilling was measured in the same $MB/K_4[Fe(CN)_6]$ solution as SEED. All of the 72 microwells on the five active electrodes of the chip were immobilized with P155. The EREB condition was N_{CV} = 5 and [c] = 1 fM corresponding to f $\sim 7.8 \times 10^{-4}$. Fresh solution was added for each EREB on each electrode. Two chips were tested to measure DPV and R_{max}. Of the ten electrodes measured;

seven had low $R_{max} \sim 1.5 \times 10^{-5}$ averaged over ~ 10 spots/electrode indicating complete MCH backfilling. Some spots on the three electrodes exhibited possible defects, with the worse electrode showing $R_{max} \sim 3 \times 10^{-5}$ averaged over 10 spots (SI, Fig. S18). The DPV current for MB redox ranged from 13 to 15 nA for good MCH backfill, while the currents for the worst backfilled electrode was ~ 100 nA (Fig. 7). At the lowest recorded current of 13 nA, the estimated current per dsDNA molecule was ~ 4.1 fA or 2.5×10^3 electrons/s. The current may be a slight overestimate because there may (still) be a possibility of some leakage current via that could contribute to the total DPV current.

For the same MB/$K_4[Fe(CN)_6]$ solution, the DPV current on a bare Au electrode was ~ 1.3 µA (SI, Fig. S19). The maximum adsorption of MB on Au is $\sim 1.5 \times 10^{14}$ molecules/cm^2 on (completely) thiolated Au.[52] Similar to DNA immobilization, assuming $\sim 1\%$ efficiency for pristine Au, the estimated redox current per MB molecule is $\sim 3.8 \times 10^2$ electrons/s, which is reasonably close to the DNA molecule electrode.

Assuming the semi-log behavior of log[c] versus redox signal by SEED[12] (Fig. 4(b)) and amperometric[11,49,50] are in the same percent binding range, then it appears that the operation was in the non-ergodic regime where the signal per duplex is dropping rapidly with square root power law.

Summary

An optical method to measure local electrochemical reaction on a 6 µm laser-spot was developed to concomitantly perform differential reflectivity (SEED-R) and interferometry (SEED-I). The local reaction appeared as peaks, R_{max} and Δ_{max} for SEED-R and SEED-I, respectively, that were linearly proportional to corresponding local redox current peak, I_{max} (by CV obtained simultaneously). For nonabsorbing redox ions, only Δ_{max} was observed. For ions that tend to adsorb to the Au electrode, the R_{max} signal was significantly dominant. Characteristics of a DNA electrode were studied, using SEED, as a function of the fraction of target ssDNA binding to immobilized ssDNA probes. The redox was exclusively from MB that binds to the dsDNA.
At constant ssDNA probe coverage of $\sim 3 \times 10^{12}$/cm^2, the fraction of binding, f was varied over three orders of magnitude from 3.30×10^{-4} to 1.28×10^{-1}. It was discovered that, the redox per dsDNA as a function of f had a remarkably sharp transition at $f = f_T \sim 1.25 \times 10^{-3}$. Below f_T, the R_{max} per molecule (due to MB redox) remained constant over an order of magnitude of f. In this regime, each molecule functioned as an individual dsDNA nanowire electrode. The signal per dsDNA was independent of number of dsDNA molecules (ergodic). In this single-molecule regime, the intermolecular distance between dsDNA molecules was estimated to be above 80 nm for 23 base pair dsDNA. Above f_T, redox per molecule rapidly decreased as $f^{-0.5}$ as classically explained by overlapping of the redox domains of individual molecules (nonergodic). The R_{max} measured at lowest f of $\sim 3.3 \times 10^{-4}$ corresponded to ~ 270 dsDNA molecules, i.e., a responsivity of 0.45 zeptomoles. Using DPV, the current per dsDNA molecule was estimated to be, ~ 4.1 fA or 2.5×10^3 electrons/s. We conclude that by comparing the SEED data with published amperometric measurements, it appears that the studies to estimate target concentration, [c] are in the nonergodic region where signal per binding changes as $f^{-0.5}$.

AUTHOR INFORMATION

Corresponding Author

* rsaraf2@unl.edu

Author Contributions

The manuscript was written through contributions of all authors. / All authors have given approval to the final version of the manuscript.
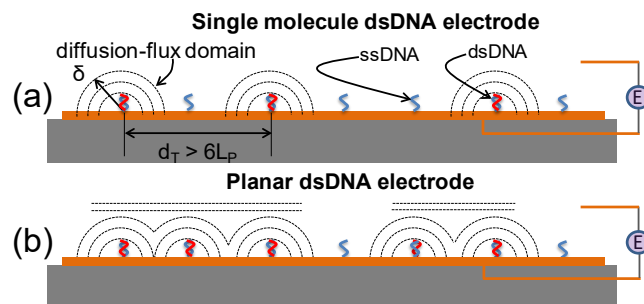
FIGURES

Figure 1: *Electrochemical nature of DNA electrode*. As the targets bind to immobilized, ssNA probes, the dsDNA will behave as (a) individual "nanoelectrodes"; and then (b) planar electrode; as binding fraction increases.
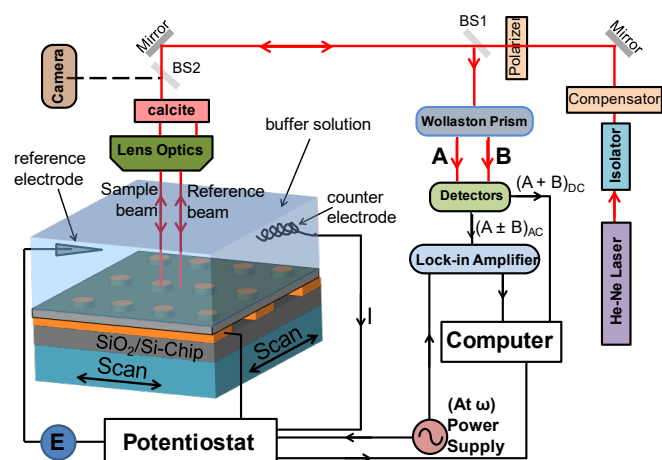
Figure 2: *Optical and Electrical set-up of SEED.* All the optical components are off the shelf. The lock-in-amplifier is from Signal Recovery (Model: 7265 DSP Lock-In Amplifier) and the potentiostat is from Autolab (Model: AUT85927, Metrohm). The He-Ne laser is 2 mW.
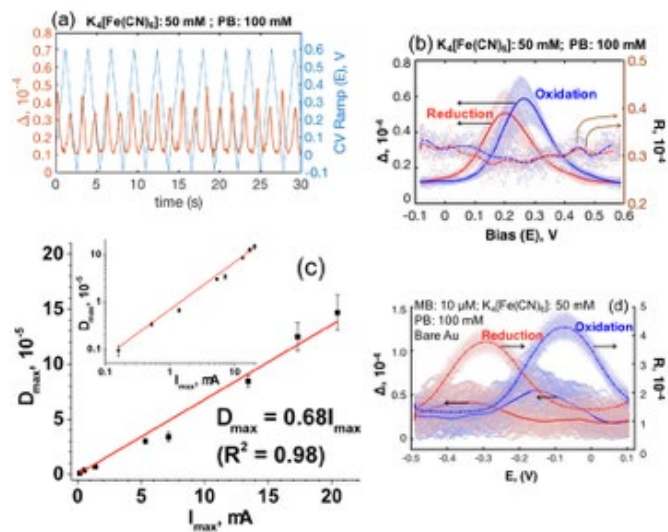

Figure 3: *SEED Signal of [Fe(CN)$_6$]$^{4-/3-}$ and MB$^+$/LMB on pristine Au.* (a) Raw data; (b) concomitantly measured SEED-I and SEED-R compiled from ~10 CV cycles; (c) concomitantly measured CV and SEED-R oxidation peaks for [c] ranging from 1 to 500 mM; and (d) Concomitantly measured SEED-I and SEED-R compiled from ~10 CV cycles similar to Fig. 4 for MB$^+$/LMB redox mediated by Fe(CN)$_6$$^{4-/3-}$.
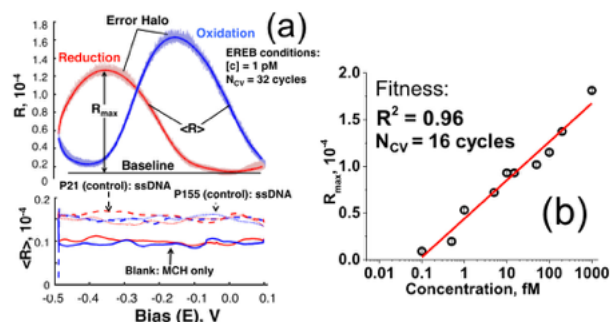
Figure 4: *Characteristics of MB redox signal from electrochemical chip.* (a) R-E behavior averaged over 10 cycles for various spots; (b) a typical calibration curve.
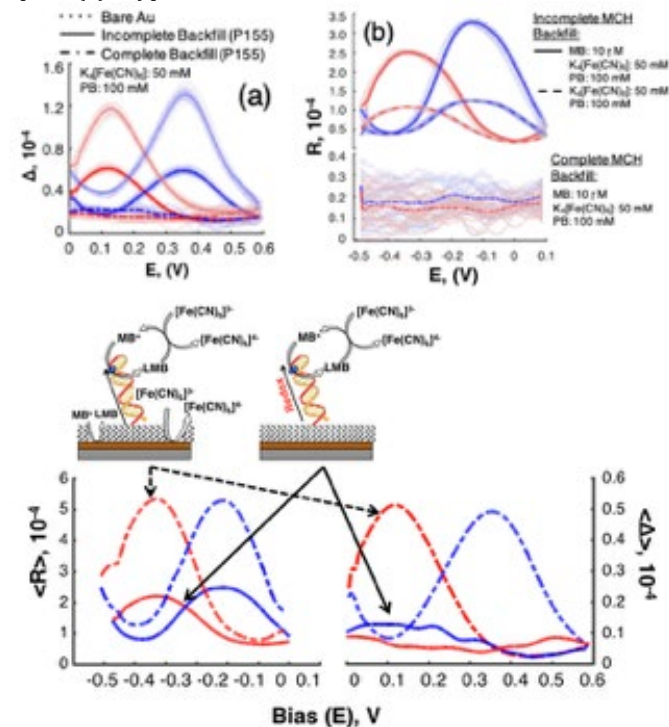
Figure 5: *Comparison of signal on complete and incomplete backfilled chip.* (a) Redox of [Fe(CN)$_6$]$^{4-/3-}$ on blank microwells. (b) Redox of MB$^+$/LMB on blank microwells on control electrode. (c) Redox on active microwells.
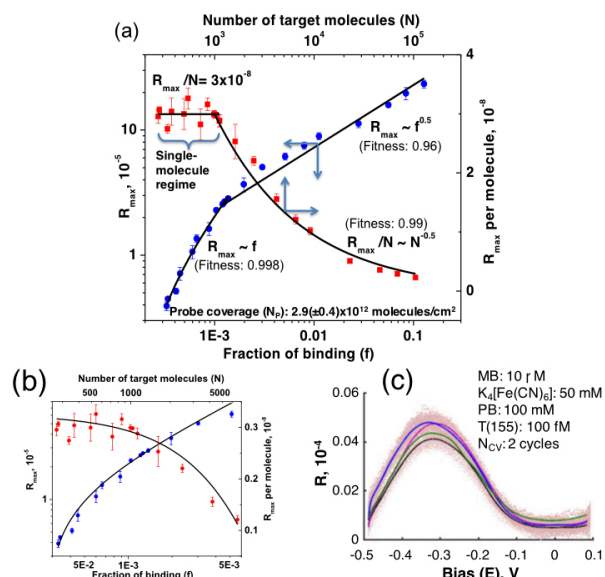
Figure 6: *Responsivity of DNA Electrode. Responsivity of DNA Electrode.* (a) A composite plot showing the two coverage regimes. The lower coverage regime is labeled as "Single molecule regime." All the curves are nonlinear or linear regression fits. (b) A magnified graph around the threshold, f$_T$. (c) The SEED-R response at five different microwells showing the MB reduction peak for the lowest coverage measured for this study (f = 3.3 x 10^{-4}).
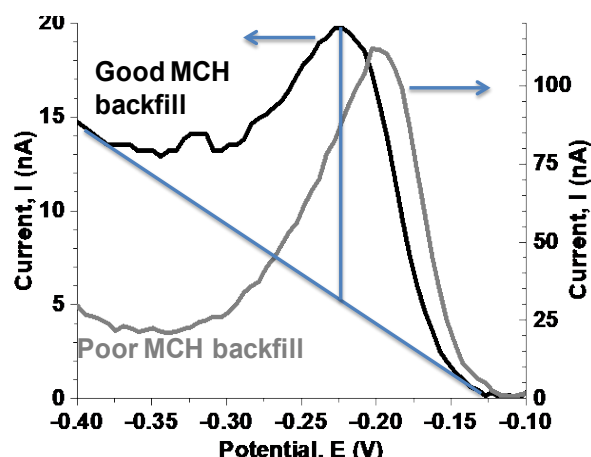
Figure 7: DPV response. Typical MB redox currents measured by DPV for two electrodes with good and (accidentally) poor MCH backfilling.

REFERENCES

1. Bain, C. D.; Troughton, E. B.; Tao, Y. T.; Evall, J.; Whitesides, G. M.; Nuzzo, R. G. Formation of Monolayer Films by the Spontaneous Assembly of Organic Thiols from Solution Onto Gold. *J. Am. Chem. Soc.* **1989,** *111*, 321-335.
2. Ferapontova, E. E. DNA Electrochemistry and Electrochemical Sensors for Nucleic Acids. *Annu. Rev. Anal. Chem., Vol 11* **2018,** *11*, 197-218.
3. Hakkinen, H. The gold-sulfur interface at the nanoscale. *Nat. Chem.* **2012,** *4*, 443-455.
4. Pensa, E.; Cortes, E.; Corthey, G.; Carro, P.; Vericat, C.; Fonticelli, M. H.; Benitez, G.; Rubert, A. A.; Salvarezza, R. C. The Chemistry of the Sulfur-Gold Interface: In Search of a Unified Model. *Acc. Chem. Res.* **2012,** *45*, 1183-1192.
5. Ulman, A. Formation and structure of self-assembled monolayers. *Chem. Rev.* **1996,** *96*, 1533-1554.
6. Gorodetsky, A. A.; Buzzeo, M. C.; Barton, J. K. DNA-Mediated Electrochemistry. *Bioconjug. Chem.* **2008,** *19*, 2285-2296.
7. Elhadj, S.; Singh, G.; Saraf, R. F. Optical properties of an immobilized DNA monolayer from 255 to 700 nm. *Langmuir* **2004,** *20*, 5539-5543.
8. Joshi, G. K.; itz-McElyea, S.; Liyanage, T.; Lawrence, K.; Mali, S.; Sardar, R.; Korc, M. Label-Free Nanoplasmonic-Based Short Noncoding RNA Sensing at Attomolar Concentrations Allows for Quantitative and Highly Specific Assay of MicroRNA-10b in Biological Fluids and Circulating Exosomes. *ACS Nano* **2015,** *9*, 11075-11089.
9. Yang, S.; Kim, H.; Lee, K. J.; Hwang, S. G.; Lim, E. K.; Jung, J.; Lee, T. J.; Park, H. S.; Kang, T.; Kim, B. Attomolar detection of extracellular microRNAs released from living prostate cancer cells by a plasmonic nanowire interstice sensor. *Nanoscale* **2017,** *9*, 17387-17395.
10. Zhou, C.; Zou, H. M.; Sun, C. J.; Ren, D. X.; Chen, J.; Li, Y. X. Signal amplification strategies for DNA-based surface plasmon resonance biosensors. *Biosens. Bioelectron.* **2018,** *117*, 678-689.
11. Das, J.; Ivanov, I.; Montermini, L.; Rak, J.; Sargent, E. H.; Kelley, S. O. An electrochemical clamp assay for direct, rapid analysis of circulating nucleic acids in serum. *Nat. Chem.* **2015,** *7*, 569-575.
12. Raghunath, S.; Prasad, A.; Tevatia, R.; Gunther, J. R.; Roy, S.; Krishnan, S.; Saraf, R. F. Quantitative Electrochemical DNA Microarray on a Monolith Electrode with Ten Attomolar Sensitivity, 100% Specificity, and Zero Background. *Chemelectrochem* **2018,** *5*, 429-433.
13. Murphy, C. J.; Arkin, M. R.; Jenkins, Y.; Ghatlia, N. D.; Bossmann, S. H.; Turro, N. J.; Barton, J. K. Long-Range Photoinduced Electr Transfer Through A Dna Helix. *Science* **1993,** *262*, 1025-1029.
14. Murphy, C. J.; Arkin, M. R.; Ghatlia, N. D.; Bossmann, S.; Turro, N. J.; Barton, J. K. Fast Photoinduced Electron-Transfer Through Dna Intercalation. *Proc. Natl. Acad. Sci. U S A* **1994,** *91*, 5315-5319.
15. Xiang, L. M.; Palma, J. L.; Bruot, C.; Mujica, V.; Ratner, M. A.; Tao, N. J. Intermediate tunnelling-hopping regime in DNA charge transport. *Nat. Chem.* **2015,** *7*, 221-226.
16. Giese, B.; Amaudrut, J.; Kohler, A. K.; Spormann, M.; Wessely, S. Direct observation of hole transfer through DNA by hopping between adenine bases and by tunnelling. *Nature* **2001,** *412*, 318-320.
17. Genereux, J. C.; Barton, J. K. Mechanisms for DNA Charge Transport. *Chem. Rev.* **2010,** *110*, 1642-1662.
18. Boon, E. M.; Ceres, D. M.; Drummond, T. G.; Hill, M. G.; Barton, J. K. Mutation detection by electrocatalysis at DNA-modified electrodes. *Nat. Biotechnol.* **2000,** *18*, 1096-1100.
19. Miyake, Y.; Togashi, H.; Tashiro, M.; Yamaguchi, H.; Oda, S.; Kudo, M.; Tanaka, Y.; Kondo, Y.; Sawa, R.; Fujimoto, T.; Machinami, T.; Ono, A. Mercury(II)-mediated formation of thymine-Hg-II-thymine base pairs in DNA duplexes. *J. Am. Chem. Soc.* **2006,** *128*, 2172-2173.
20. Kelley, S. O.; Barton, J. K.; Jackson, N. M.; Hill, M. G. Electrochemistry of methylene blue bound to a DNA-modified electrode. *Bioconjug. Chem.* **1997,** *8*, 31-37.
21. Yang, H.; Hui, A.; Pampalakis, G.; Soleymani, L.; Liu, F. F.; Sargent, E. H.; Kelley, S. O. Direct, Electronic MicroRNA Detection for the Rapid Determination of Differential Expression Profiles. *Angew. Chem.. Int. Ed.* **2009,** *48*, 8461-8464.
22. Yu, C. C.; Lee, S. W.; Ong, J.; Moore, D.; Saraf, R. F. Single Electron Transistor in Aqueous Media. *Adv. Mater.* **2013,** *25*, 3079-3084.
23. Levicky, R.; Herne, T. M.; Tarlov, M. J.; Satija, S. K. Using self-assembly to control the structure of DNA monolayers on gold: A neutron reflectivity study. *J. Am. Chem. Soc.* **1998,** *120*, 9787-9792.
24. Herne, T. M.; Tarlov, M. J. Characterization of DNA probes immobilized on gold surfaces. *J. Am. Chem. Soc.* **1997,** *119*, 8916-8920.
25. Lee, C. Y.; Gong, P.; Harbers, G. M.; Grainger, D. W.; Castner, D. G.; Gamble, L. J. Surface coverage and structure of mixed DNA/alkylthiol monolayers on gold: Characterization by XPS, NEXAFS, and fluorescence intensity measurements. *Anal. Chem.* **2006,** *78*, 3316-3325.
26. Josephs, E. A.; Ye, T. A Single-Molecule View of Conformational Switching of DNA Tethered to a Gold Electrode. *J. Am. Chem. Soc.* **2012,** *134*, 10021-10030.
27. Kaiser, W.; Rant, U. Conformations of End-Tethered DNA Molecules on Gold Surfaces: Influences of Applied Electric Potential, Electrolyte Screening, and Temperature. *J. Am. Chem. Soc.* **2010,** *132*, 7935-7945.
28. Tymoczko, J.; Schuhmann, W.; Gebala, M. Electrical Potential-Assisted DNA Hybridization. How to Mitigate Electrostatics for Surface DNA Hybridization. *ACS Appl. Mater. Inter.* **2014,** *6*, 21851-21858.
29. Wong, I. Y.; Melosh, N. A. Directed Hybridization and Melting of DNA Linkers using Counterion-Screened Electric Fields. *Nano Lett.* **2009,** *9*, 3521-3526.
30. Bardea, A.; Patolsky, F.; Dagan, A.; Willner, I. Sensing and amplification of oligonucleotide-DNA interactions by means of impedance spectroscopy: a route to a Tay-Sachs sensor. *Chem. Comm* **1999,** (1), 21-22.
31. Keighley, S. D.; Li, P.; Estrela, P.; Mighorato, P. Optimization of DNA immobilization on gold electrodes for label-free detection by electrochemical impedance spectroscopy. *Biosens. Bioelectron.* **2008,** *23* (8), 1291-1297.
32. Souteyrand, E.; Cloarec, J. P.; Martin, J. R.; Wilson, C.; Lawrence, I.; Mikkelsen, S.; Lawrence, M. F. Direct detection of the

hybridization of synthetic homo-oligomer DNA sequences by field effect. *J. Phys. Chem. B* **1997,** *101* (15), 2980-2985.

33. Steel, A. B.; Herne, T. M.; Tarlov, M. J. Electrochemical quantitation of DNA immobilized on gold. *Anal. Chem.* **1998,** *70* (22), 4670-4677.

34. Peterson, A. W.; Heaton, R. J.; Georgiadis, R. M. The effect of surface probe density on DNA hybridization. *Nucleic Acids Res.* **2001,** *29* (24), 5163-5168.

35. Arinaga, K.; Rant, U.; Knezevic, J.; Pringsheim, E.; Tornow, M.; Fujita, S.; Abstreiter, G.; Yokoyama, N. Controlling the surface density of DNA on gold by electrically induced desorption. *Biosens. Bioelectron.* **2007,** *23* (3), 326-331.

36. Ferrario, A.; Scaramuzza, M.; Pasqualotto, E.; De Toni, A.; Paccagnella, A. Coadsorption optimization of DNA in binary self-assembled monolayer on gold electrode for electrochemical detection of oligonucleotide sequences. *J. Electroanal. Chem.* **2013,** *689*, 57-62.

37. Lin, M. H.; Song, P.; Zhou, G. B.; Zuo, X. L.; Aldalbahi, A.; Lou, X. D.; Shi, J. Y.; Fan, C. H. Electrochemical detection of nucleic acids, proteins, small molecules and cells using a DNA-nanostructure-based universal biosensing platform. *Nature Protocols* **2016,** *11* (7), 1244-1263.

38. Davies, T. J.; Compton, R. G. The cyclic and linear sweep voltammetry of regular and random arrays of microdisc electrodes: Theory. *J. Electroanal. Chem.* **2005,** *585* (1), 63-82.

39. LaFratta, C. N.; Walt, D. R. Very high density sensing arrays. *Chem. Rev.* **2008,** *108*, 614-637.

40. Saito Y. A Theoretical Study on the Diffusion Current at the Stationary Electrodes of Circular and Narrow Band Types. *Rev. Polarogr.* **1968,** *15*, 177-187.

41. Hanken, D. G.; Corn, R. M. Electric fields and interference effects inside noncentrosymmetric multilayer films at electrode surfaces from electrochemically modulated surface plasmon resonance experiments. *Anal. Chem.* **1997,** *69* (18), 3665-3673.

42. Iwasaki, Y.; Horiuchi, T.; Niwa, O. Detection of electrochemical enzymatic reactions by surface plasmon resonance measurement. *Anal. Chem.* **2001,** *73* (7), 1595-1598.

43. Shan, X. N.; Patel, U.; Wang, S. P.; Iglesias, R.; Tao, N. J. Imaging Local Electrochemical Current via Surface Plasmon Resonance. *Science* **2010,** *327* (5971), 1363-1366.

44. Singh, G.; Saraf, R. F. Direct measurement of ion accumulation at the electrode electrolyte interface under an oscillatory electric field. *J. Phys. Chem. B* **2006,** *110*, 12581-12587.

45. Lee, S. W.; Lopez, J.; Saraf, R. F. Fabrication and Properties of Redox Ion Doped Few Monolayer Thick Polyelectrolyte Film for Electrochemical Biosensors at High Sensitivity and Specificity. *Electroanalysis* **2013,** *25*, 1557-1566.

46. Lee, S. W.; Lopez, J.; Saraf, R. F. Direct mapping of local redox current density on a monolith electrode by laser scanning. *Biosens. Bioelectron.* **2013,** *47*, 408-414.

47. Singh, G.; Moore, D.; Saraf, R. F. Localized Electrochemistry on a 10 mu m Spot on a Monolith Large Electrode: An Avenue for Electrochemical Microarray Analysis. *Anal. Chem.* **2009,** *81*, 6055-6060.

48. Barner, B. J.; Corn, R. M. Electrochemical and Vibrational Spectroscopic Studies of Coadsorption - Formation of Mixed Monolayers of Methylene-Blue and Long-Chain Dithioethers at Sulfur-Modified Polycrystalline Gold Surfaces. *Langmuir* **1990,** *6*, 1023-1030.

49. Labib, M.; Khan, N.; Ghobadloo, S. M.; Cheng, J.; Pezacki, J. P.; Berezovski, M. V. Three-Mode Electrochemical Sensing of Ultralow MicroRNA Levels. *J. Am. Chem. Soc.* **2013,** *135*, 3027-3038.

50. Wang, Z. W.; Zhang, J.; Guo, Y.; Wu, X. Y.; Yang, W. J.; Xu, L. J.; Chen, J. H.; Fu, F. F. A novel electrically magnetic-controllable electrochemical biosensor for the ultra sensitive and specific detection of attomolar level oral cancer-related microRNA. *Biosens. Bioelectron.* **2013,** *45*, 108-113.

51. Roy, S.; Prasad, A.; Tevatia, R.; Saraf, R. F. Heavy metal ion detection on a microspot electrode using an optical electrochemical probe. *Electrochem. Commun.* **2018,** *86*, 94-98.

52. Clavilier, J.; Svetlicic, V.; Zutic, V.; Ruscic, B.; Chevalet, J. Electrochemical Separation of the Inner Monolayer in Methylene-Blue Leucomethylene Blue Conductive Films Induced by A Sulfur-Modified Gold Surface. *J. Electroanal. Chem.* **1988,** *250*, 427-442.

53. Bard, A. J.; Faulkner, L. R. *Electrochemical Methods: Fundamentals and Applications;* 2nd ed.; J. Wiley & Sons, New York: 2001.

54. Kakiuchi, T.; Usui, H.; Hobara, D.; Yamamoto, M. Voltammetric properties of the reductive desorption of alkanethiol self-assembled monolayers from a metal surface. *Langmuir* **2002,** *18*, 5231-5238.

Electrochemical Characteristics of DNA Modified Electrode as a Function of Percent Binding

Rahul Tevatia,[a] Abhijeet Prasad,[b] Ravi F. Saraf*[b],[c]

[a] Vajra Instruments, Inc, Lincoln, NE 68512

[b] Department of Chemical and Biomolecular Engineering, University of Nebraska-Lincoln, NE 68512;

[c] Nebraska Center for Material and Nanoscience, University of Nebraska-Lincoln, NE 68512

* rsaraf2@unl.edu

SI Table of Contents:

S1. Chemicals and DNA handling

The photoresist SU8 and developer were purchased from Microchem. Acetone, ethanol, hydrogen peroxide (40% v/v), concentrated sulfuric acid, and cyclopentanone were chemical grade and purchased from Sigma-Aldrich. Tris(2-carboxyethyl)phosphine hydrochloride (TCEP), 1-mercapto-6-hexanol (MCH), potassium ferrocyanide, and methylene blue (MB) were purchased from Sigma-Aldrich. Reference electrodes required a silver wire, reference filling, and reference electrode storage solutions (Sigma-Aldrich). Phosphate monobasic and phosphate dibasic (Sigma-Aldrich) were used to prepare 1.0 M stock solution of phosphate buffer (the amount was calculated using the Henderson–Hasselbalch equation for a final pH = 7.6). Reagents for PCR, SYBR® Green miRNA assay were purchased from Clontech Lab Inc. DNA/RNA probes and targets with or without thiol or Cy3 modifications were synthesized by Integrated DNA Technologies, Inc (IDT).

All DNA/RNA were received in lyophilized form and substituted with DNase/Rnase-free water to 1 mM final concentration. These stocks were stored at -20 °C. From 1 mM master stocks, 10 μM processed probes or unmodified targets were aliquot in 10 μl and stored at -20 °C. Each 10-μl vial was used once to avoid any potential damage to the nucleic acids caused by repeated freeze-thaw cycles.

S2. Chip Fabrication, Spotting, EREB and MCH Backfilling

There were four steps to make the DNA electrode in an array of seventy-two 50 μm diameter microwells by spotting followed by binding and backfilling steps (Figure 2(b)). First, 50-μm diameter microwells were patterned by photolithography using 500-nm thick SU8 photoresist (Figure S1 and S2(a)). Each of the five electrodes had a matrix of 6 x 12 microwells, while the two small electrodes had three microwells each. Second, the chip was exposed to oxygen (O_2) plasma (at 500 mTorr, 65 W) for 60 sec to clean the remaining SU8; and ssDNA probes were spotted on each individual microwell using a home-built spotter (Figure S2(b) and S3(a)). Third, the binding was performed by applying a potential between the electrode and the solution containing the target, miR-155 (Figure S2(c)). The five large electrodes were subjected to the probe-target binding process, while no potential to bind was applied to the smaller electrodes. Thus, the microwells on the smaller electrode served as controls where no binding occurred. Fourth, the exposed Au electrode was backfilled with MCH (Figure S2(d)). As described, the binding was performed electrochemically and backfilling was a two-step process to ensure complete passivation of the electrode surrounding the DNA. Each of the four steps is discussed below.
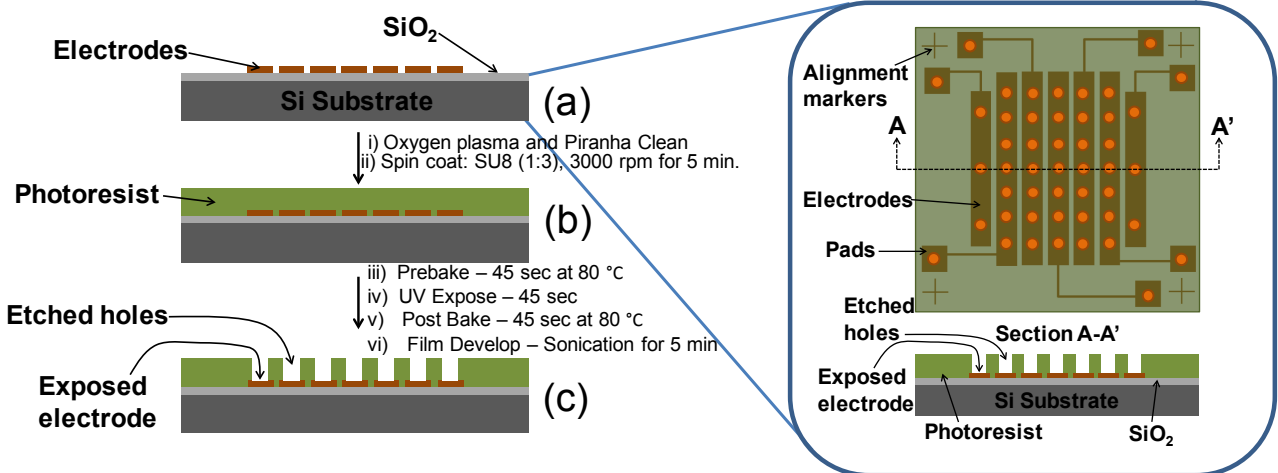
Figure S1: Cross-sectional view of the chip defined by A-A' in Figure 2. Broadly, the photolithography had the following steps: (a) initial chip with electrodes; (b) after spin coating SU-8 photoresist; and (c) the chip after exposure to UV light and development to obtain a pattern of etched holes. Right: Schematic of the chip with electrodes, connecting pads and microwells. For the study there are 3 and 72 microwells on the 2 control and 5 active electrodes.
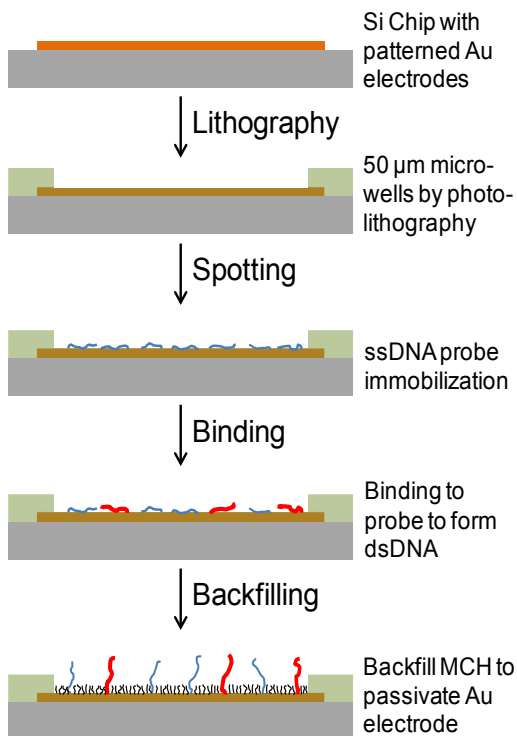

Figure S2: The four steps used to immobilize DNA on a typical microwell.

a) Step 1: Chip fabrication – The microarray was made on a 1.2 by 1.2 cm silicon (Si) chip with ~200 nm silicon dioxide (SiO_2) (thermal oxide) to provide an insulating surface. Gold (Au) electrodes and accompanying circuitry for power and signal on the chip were patterned at the wafer level using standard photolithography followed by dicing of the wafer to make chips. The electrodes were 40 nm Au on 10 nm titanium (Ti) on silica. The Ti was used to promote adhesion between the silica and Au. The chip was coated with SU8 photoresist to make 72 and 3 holes of 50 µm diameter on the longer and shorter electrodes, respectively, using a standard photolithography process (Figure S1). Briefly, the chip was cleaned in acetone, water, and ethanol followed by oxygen (O_2) plasma and subsequently immersed in piranha solution for ~60 sec. The chip was dried by blowing clean nitrogen (N_2) through a 0.2 µm Millipore™ filter. Photoresist SU8 (MicroChem 2025) was diluted by adding three times the volume of cyclopentanone which was spin cast onto the chip at 3,000 rpm for 60 sec to produce a ~500-nm thick film. The chip was prebaked for 45 s at 80 °C. The film was exposed to xenon (Xe) light (300 W) for 45 s through a contact mask with a chromium (Cr) metalized pattern on quartz. The chip was post-baked for 45 s at 80 °C and developed in MicroChem SU8 developer in a sonicator for 5 minutes. The chip was washed with water/isopropanol for ~60 s and hard baked at 180 °C for 1 hr. The resulting pattern on each electrode was a microarray of 50 µm holes exposing the underlying Au electrode

b) Step 2: Probe Spotting – After photolithography, the chip was exposed to O_2 plasma to clean the leftover organics and expose the electrode in the microwell. The chip was then hard baked at 180 °C to improve the adhesion and make the SU8 (back to being) hydrophobic. Individual solutions of the probes P155 and P21, were prepared in a volumetric ratio of one part of 1 mM ssDNA probe and five parts of 500 mM TCEP solution at pH 7. The solution was mixed and incubated at 25 °C for 1 hour. The solution was subsequently diluted with 1M PB at pH 7.6 to obtain a final concentration of 2.5 µM probe. The TCEP was utilized to cleave the disulfide linkages between the thio-groups among the probe molecules. The thiolated probe solution was spotted on each microwell using a 20 µm capillary pin (Arrayit® 20 µm tip) with the sample on a computer-controlled motorized X-Y stage arm and machine vision (see Figure S3(a)). The drop was released by surface tension on the hydrophilic microwell. The drop was confined to the microwell owing to the hydrophobic nature of surrounding SU8 resist (see Figure S3(b)). The probe immobilization was allowed for 2 hours. The chip was cooled to 10 °C and maintained in a humid environment to avoid evaporation of the approximate 100 nL drop during the immobilization process. Throughout the study on the short (control) electrode, the three microwells had no probe (i.e., blank), P155, and P21, respectively. The other five (active) electrodes had all of the 72 microwells immobilized with P155.
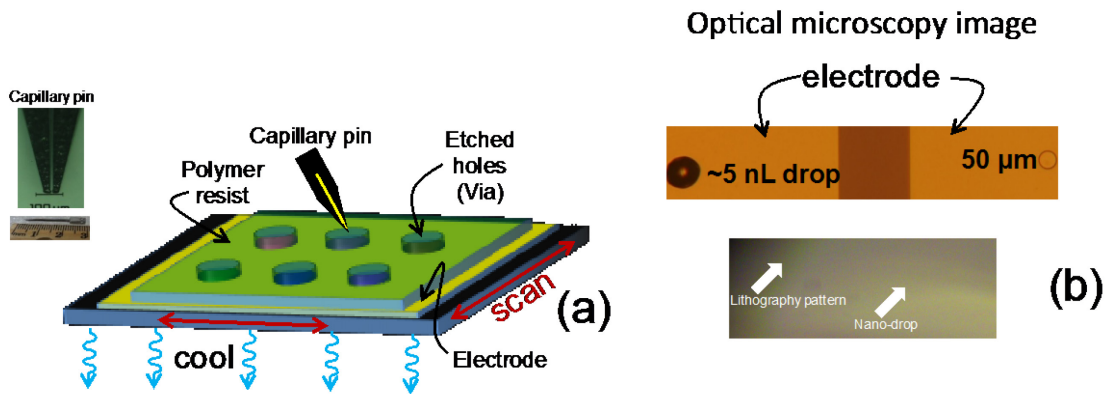
Figure S3: DNA probe immobilization (a) The schematic of the spotting. The inset is the capillary pin used to dispense the solution. (b) An optical image of the ssDNA probe solution droplet confined to the microwell. The drop was held by surface tension.

c) <u>Step 3: Electrochemical Redox Enhanced Binding (EREB)</u> – The binding was performed electrochemically using a potentiostat (Autolab, Metrohm) in a cyclic voltammetry (CV) setup on each of the five larger electrodes using a silver/ silver chloride (Ag/AgCl) reference electrode (RE) (Figure S4). The CV ramp was from -0.4 to +0.3 V at a rate of, s = 0.05 V/s. The solution had synthetic miR-155 target of concentration [c], in 100 mM PB (pH 7.6) with 50 mM $K_4[Fe(CN)_6]$. The amount of binding was regulated in two ways: (i) [c]; and (ii) number of CV ramp cycles, N_{CV}. For a low amount of binding, [c] was fixed at 100 fM; and N_{CV} during EREB was varied from 2 to 28 cycles. For a high amount of binding, N_{CV} was constant at 32, while [c] was varied from 10^2 to 10^3 fM. As the electrochemical binding in this study was <15 min (at maximum N_{CV} = 32 cycles), compared to ~18 hrs for conventional process by diffusion, there was no significant binding at N_{CV} = 0. Thus, EREB on each active electrode can be considered to be an isolated experiment. For small control electrodes, N_{CV} = 0. As a result, five EREB conditions were measured for each chip. The volume of the solution for EREB was 500 μL. The chamber was disassembled and washed after each EREB cycle.
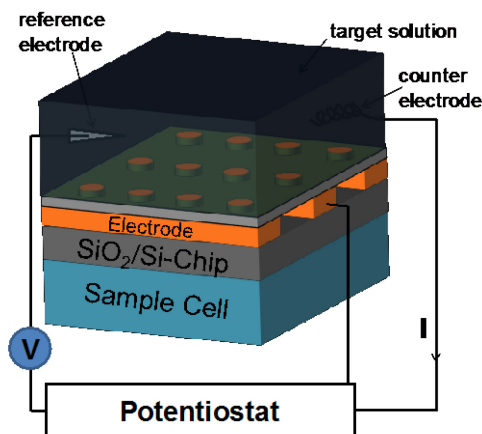

Figure S4: A schematic of the three-electrode setup for EREB process. The reference electrode was silver/silver chloride (Ag/AgCl), and the counter electrode was platinum (Pt) wire. CV between one of the five "active electrode" and solution was applied for a fixed number of cycles, N_{CV}.

d) Step 4: MCH backfill – Backfilling was one of the critical aspects of the fabrication. The MCH immobilization (i.e., backfilling) was performed in two steps. The chip was exposed to vapors from a 0.5-mL solution of 10 mM MCH in DNAse/RNAse-free water at 37 °C for 10 hr. The chip was dry with no condensation of water during the process. After rinsing in autoclaved deionized (DI) water, the chip was then immersed in a 2 mL solution of 10 mM MCH in 30% HPLC grade ethanol for 3 hours with vigorous shaking at 100 rpm in an incubator at 37 °C. The second incubation step is critical to plug the small holes in the MCH layer. The chip was subsequently rinsed and immersed in solution for SEED measurement.

S3. qPCR Analysis for Probe Coverage and Fraction Target Binding

The SYBR$^®$ Green method (Clontech Lab., Inc) was adopted to perform the cDNA synthesis and quantitative polymerase chain reaction (qPCR) measurements (QuantStudio$^™$ 3 RT-PCR, ABI, USA). Briefly, 3.75 µL of a standard solution with a known concentration was added to reverse a transcriptase buffer and enzyme (the final reaction volume was 10 µL). The reverse transcriptase reaction was allowed to incubate at 37 °C for one hour, followed by denaturation of the RT enzyme at 85 °C for five minutes. The synthesized cDNA was diluted by 10-fold. A 0.8 µL portion was added to the master stock (SYBR Advantage Premix, ROX, miRNA-specific 5' and 3' primers) resulting in the final volume of 10 µL. Melting curves on qPCR products were also generated to confirm the specificity of the amplification. After qPCR, the data was analyzed while setting the threshold fluorescence to a constant value of 0.059 arbitrary units. The threshold was set to a constant for biological replicates. Based on Ct values, the number of probes or targets was calculated from the standard curve.

Figure S5 shows the standard curve for both the probe and target measure from known amount of synthetic ssDNA molecules in the RT-mixture.
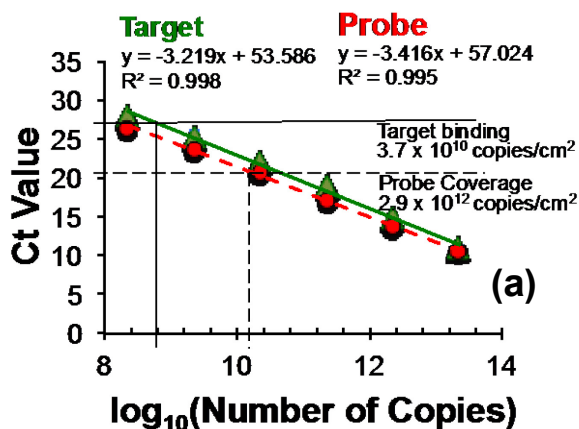

Figure S5: The standard curve of the probe and target for SYBR-Green qPCR. The copy number is the number of molecules in the RT mix for cDNA conversion. Below 10^6 number of copies, the CT value the curve becomes nonlinear.
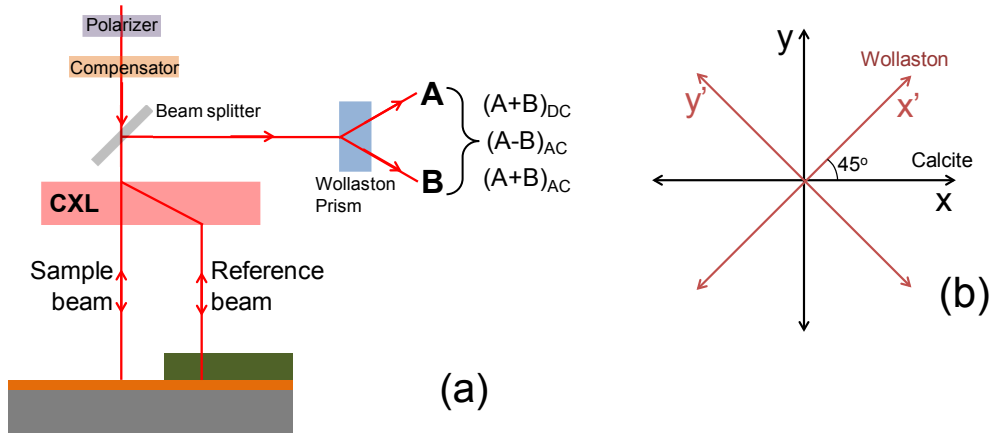
Figure S6: Beam path in SEED. a) The input polarized light is split into two beams by CXL. b) The output beam is then split by a Wollaston prism with polarization at 45º with respect to the input beam polarization by CXL.

S4. The Analysis of SEED Optics

Phase modulation of the reflected light

As shown in Figure S6(a), the polarized light is split into sample and reference beams, of the electric field given by

$$E_r = r_o e^{i\left(\frac{2\pi c}{\lambda}\right)t} \tag{1a}$$

$$E_s = s_o e^{i\left(\left(\frac{2\pi c}{\lambda}\right)t+\psi\right)} \tag{1b}$$

where, ω_o is the frequency of the light; ψ is a phase introduced by the compensator (and the SU8); and the polarization of the incident beam such that amplitudes (i.e., intensities) $r_o = s_o$.

Because of the AC potential at ω, the path length, p.l. modulated as

$$p.l. = \left(\int_0^\kappa \frac{dn_+}{dc}\delta c_+ dx \int_0^\kappa \frac{dn_-}{dc}\delta c_- dx\right)cos\omega t = z_o cos\omega t \tag{2}$$

where, dn/dc is the differential refractive index, a constant, δc is the amplitude of oscillation of the ions in the interfacial layer due to the AC potential, κ, is the penetration depth of the electric field emanating from the electrode into the solution, and z_o is the amplitude of the path length oscillation due to the AC potential. Usually, the polarizability of the anion is significantly larger due to uncompensated electrons, thus, e z_o is governed by concentration of anions, c_- compared to cations, c_+, in the solution. Assuming the system to be linear, a good assumption is that the second order signal at 2ω is very small, the amplitude of path length oscillation at ω is given by

$$z_o \approx \frac{dn_-}{dc}\kappa\langle\delta c_-\rangle \tag{3}$$

where, <...> is the spatial average. The resultant phase modulation due to the path length modulation, z_o is

$$\phi = \frac{2\pi}{\lambda}z_o\cos\omega t \tag{4}$$

where, λ = 633 nm is the wavelength of the He-Ne laser beam.

Thus, the optical electric fields (in Eq. (1)), after reflection, is given by

$$E_r = r_o e^{i\left(\frac{2\pi c}{\lambda}\right)t} \tag{5a}$$

$$E_s = r_o e^{i\left[\left(\frac{2\pi c}{\lambda}\right)t+\psi+\phi\right]} \tag{5b}$$

Furthermore, another phase difference, α, is introduced due to reflectivity at the electrolyte/electrode interface relative to the SU8/electrode interface. Thus, the reflected light will be

$$E_r = r_o e^{i\left(\frac{2\pi c}{\lambda}\right)t} \tag{6a}$$

$$E_s = Rr_o e^{i\left[\left(\frac{2\pi c}{\lambda}\right)t+\psi+\phi+\alpha\right]} \tag{6b}$$

where, R is the reflectivity of the sample beam relative to the (constant) reflectivity of the reference beam. As a result, the reflectivity to the reference beam is set to 1. From Fresnel's law, the complex reflectivity amplitude is given by

$$\mathbb{R} = \frac{N_1-N_2}{N_1+N_2} = Re^{i\alpha} \tag{7}$$

where, $N_1 = \langle n_1 - ik_1\rangle$ and $N_2 = n_2 - ik_2$ are complex refractive indices of the electrolyte at the interface and electrode, respectively. Typically, the Fresnel reflectivity, R_F, due to MB, $\langle n_1\rangle\sim$ 1.5 and $\langle k_1\rangle \sim 10^{-3}$; and 633 nm for the Au electrode, $n_2 \sim 0.21$ and $k_2 \sim$ 3.24, Eq. (7) can be approximated as,

$$R = R_F = 1 - \frac{2\langle n_1\rangle n_2}{\langle n_1\rangle^2+k_2^2} = 1 - K'_o \tag{8a}$$

$$\alpha = \frac{2\langle n_1\rangle}{k_2} \tag{8b}$$

To derive Eq. (8) from Eq. (7) we have assumed, $k_1 \ll k_2$, $(\langle n_1\rangle)^2 \gg (n_2)^2$, and $\langle n_1\rangle k_2 \gg n_2 k_1$. To note is that for typical values of the solution and the electrode, $K'_o \sim 0.05$ and $\alpha \sim 0.86$ radians.

The AC potential will also modulate the reflectivity via the oscillation of the ions in the vicinity of the electrode surface. As the Fermi level of Au is lower than the solution,[1] the

interface (very close to the surface) will primarily have anions. Thus, in the vicinity of the surface, the refractive index of the solution due to the AC potential is given by,

$$n_s = \langle n_{1s} \rangle + \frac{dn_-}{dc} \langle \delta c_s \rangle \cos\omega t = \langle n_{1s} \rangle + \delta n_s \cos\omega t \tag{9}$$

where, constant $\langle n_{1s} \rangle$ is the (spatially averaged) effective refractive index of the solution at the Au surface, and $\langle \delta c_s \rangle$ is the spatially averaged amplitude of oscillation of the anions at the surface. Thus, substituting $\langle n_1 \rangle = \langle n_{1s} \rangle$ in Eq. 8, the oscillation in the Fresnel reflectivity due to the AC potential can be obtained as,

$$R_F = 1 - \frac{2\langle n_{1s} \rangle n_2}{\langle n_{1s} \rangle^2 + k_2^2} - 2n_2 \frac{(k_2^2 - \langle n_{1s} \rangle^2)}{(\langle n_{1s} \rangle^2 + k_2^2)^2} \delta n_s \cos\omega t$$

$$= 1 - K_o - K_1 \delta n_s \cos\omega t = 1 - K_o - R_o \cos\omega t \tag{10a}$$

$$\alpha = \frac{2\langle n_{1s} \rangle}{k_2} + \frac{2\delta n_s}{k_2} \cos\omega t \tag{10b}$$

In summary, the amplitude of the reflected beam is given by, Eq. 6, where, ϕ is given by Eq. (4) and (3); R_F and α are given by Eq. (10) and (9); and ψ is a constant phase angle regulated by the compensator for nulling as discussed below.

Signal Detection

Next, we calculate the intensities, A and B at the two detectors after superposition (i.e., interference) occurs in the CXL. (This is advantageous because of the reduction in thermal noise that would occur if interference occurred in air.) To reduce thermal noise further, the CXL is mounted in an insulating foam. The output beam is then split by a Wollaston prism with polarization at 45° with respect to the CXL (Figure S6(b)). As a result, the amplitudes on detectors A and B are

$$E_A = \frac{1}{\sqrt{2}} (E_r + E_s) \tag{11a}$$

$$E_B = \frac{1}{\sqrt{2}} (E_r - E_s) \tag{11b}$$

where, E_r and E_s are given by Eq. (6) with all of the phases and reflectivity given be Eq. (4) and (10). Thus, the power (i.e., the intensity of the light), that is measured on each detector given by, $E_A(E_A)^*$ and $E_B(E_B)^*$, is

$$A = \frac{1}{2} [r_o^2 + R_o^2 r_o^2 + 2R_o r_o^2 \cos(\psi + \phi + \alpha)] \tag{12a}$$

$$B = \frac{1}{2} [r_o^2 + R_o^2 r_o^2 - 2R_o r_o^2 \cos(\psi + \phi + \alpha)] \tag{12b}$$

The Nulling

The intensity measured on the two detectors (Eq. (12)) have both AC and DC

components. By adding and subtracting the two differential signals (using simple hardware), the signal from Eq. (12) becomes,

$$(A - B)_{AC+DC} = 2R_o cos(\psi + \phi + \alpha) \qquad (13a)$$

$$(A + B)_{AC+DC} = 1 + R_o^2 \qquad (13b)$$

The added and subtracted AC signal after amplification by the lock-in amplifier tuned at ω (see Figure 3 in main MS and Figure S6), and the DC signal is directly hardwired into the computer. As noted above, the AC oscillations are very small to maintain the linearity of the measurement. The higher harmonics (that can directly be measured from the lock-in-amplifier) of ω are at least three orders of magnitude lower. As a result, the AC amplitude of R_F, ϕ, and α are <<1. By collecting only the first harmonic term at ω, from Eqs. (8), (10), and (13),

$$\left| \frac{(A-B)_{AC}}{(A+B)_{DC}} \right| = 2(1 - K_o)cos(\psi + \phi + \alpha) \qquad (14a)$$

$$\left| \frac{(A+B)_{AC}}{(A+B)_{DC}} \right| = 2(1 - K_o)K_1 \delta n_s \qquad (14b)$$

where, the normalizing DC signal, $(A+B)_{DC}$, measured by passing the signal through a low pass filter is $(r_o)^2$. To note is that the AC oscillation term, $K_1 n_s cos(\omega t)$, in Eq. (10) is dropped because it will lead to second harmonics.

Away from the redox, the compensator is adjusted such that ψ = π/2. This is obtained by adjusting the compensator so that the baseline is minimum and flat. The important aspect of the optics is that because the two beams are always close, <100 μm apart, the thermal environment is similar, leading to very stable ψ that does not require feedback during the measurement. For ψ = π/2 and dropping higher harmonic terms and considering that the oscillation amplitudes are small, the normalized output raw signal at the computer measured in real time (see Figure 3(a)) becomes,

$$\left| \frac{(A-B)_{AC}}{(A+B)_{DC}} \right| = \Delta = \frac{4\pi}{\lambda} z_o + \frac{4}{k_2} \delta n_s \text{ (SEED-I raw signal)} \qquad (15)$$

$$\left| \frac{(A+B)_{AC}}{(A+B)_{DC}} \right| = R = 2K_1 \delta n_s \qquad \text{(SEED-R raw signal)} \qquad (16)$$

Both R and Δ are dimensionless quantities that may now be compared to understand the observation made in each mode.

General remarks:

- The interferometry signal, i.e., SEED-I in Eq. (15) is a linear combination of the SEED-I and SEED-R signals, while SEED-R measures near-surface phenomena exclusively.

- There is some amount of amplification in the SEED-I signal because z_o

includes oscillations extending "deep" into the solution, while the signal is from the near-surface process for reflectivity.

- SEED-I should always yield a signal, while the signal may be weak for conventional redox processes in SEED-R where the redox ions are in the solution.

- SEED-R may be more sensitive to redox ions confined to the surface.

- In principle, only one beam is needed for SEED-R.

- Both $<\delta c>$ (in Eq. (3)) and $<\delta c_s>$ (in Eq. 9) are linearly proportional to the (local) redox current, where the proportional constant will have to be calibrated.

S5. Figures S7 to S16

Following are nine illustrations that aid the discussion in the main manuscript.
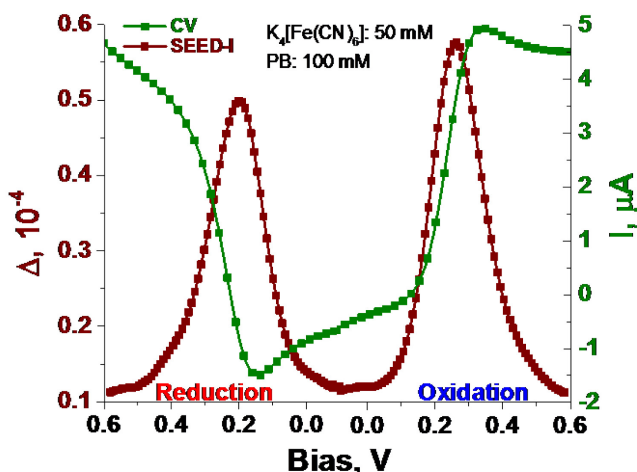
Figure S7: Using the setup in Figure 2, the CV and SEED-I were concomitantly measured for 50 mM $K_4[Fe(CN)_6]$ in 100 mM PB at a ramp rate of, s = 0.05 V/s. The SEED-R signal was from the 6-μm spot of area 2.83 x 10^{-7} cm^2; and the CV signal was from all of the 72 microwells with a combined area of 1.41 x 10^{-3} cm^2. Thus, the area of SEED-I was 5 x 10^3-fold smaller than CV.
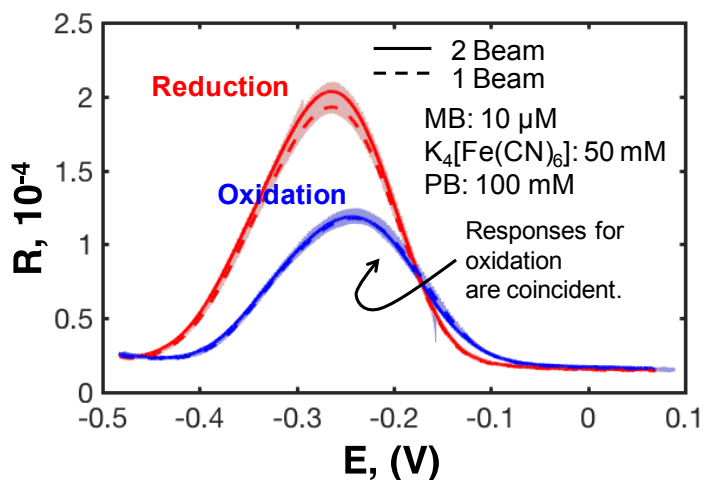
Figure S8: Comparison between SEED-R signal with two beam (i.e., Figure 2) and clipping the reference beam after the CXL.
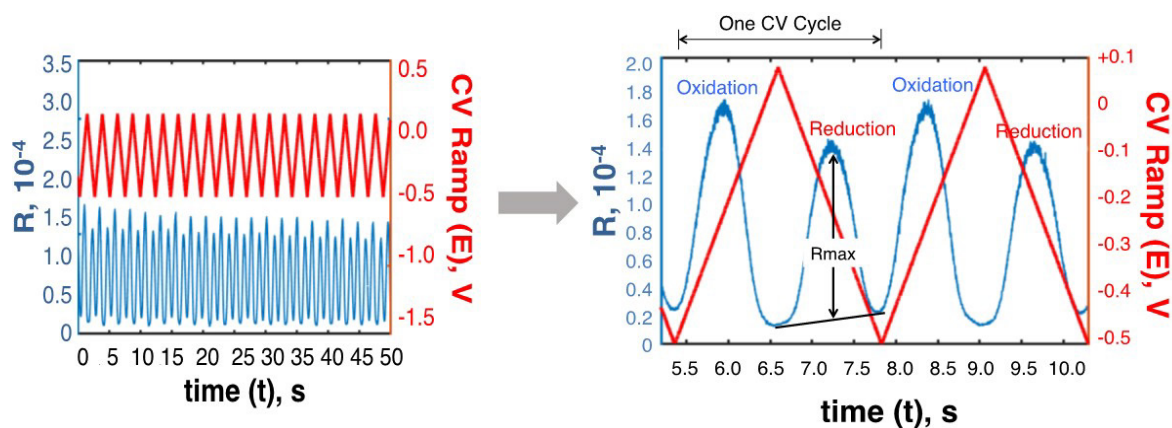

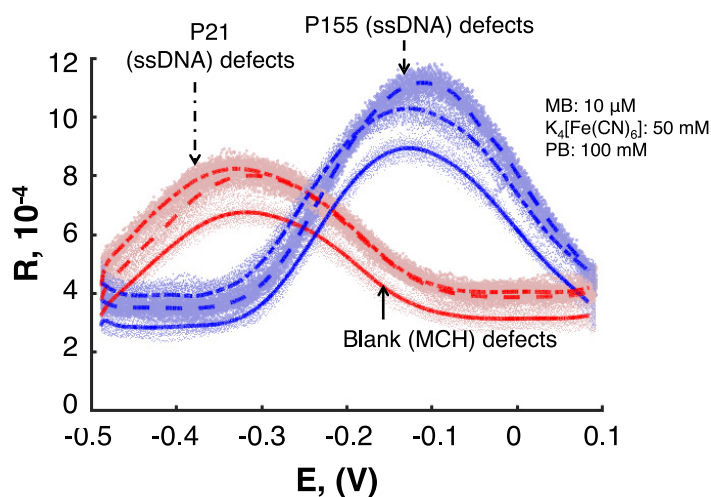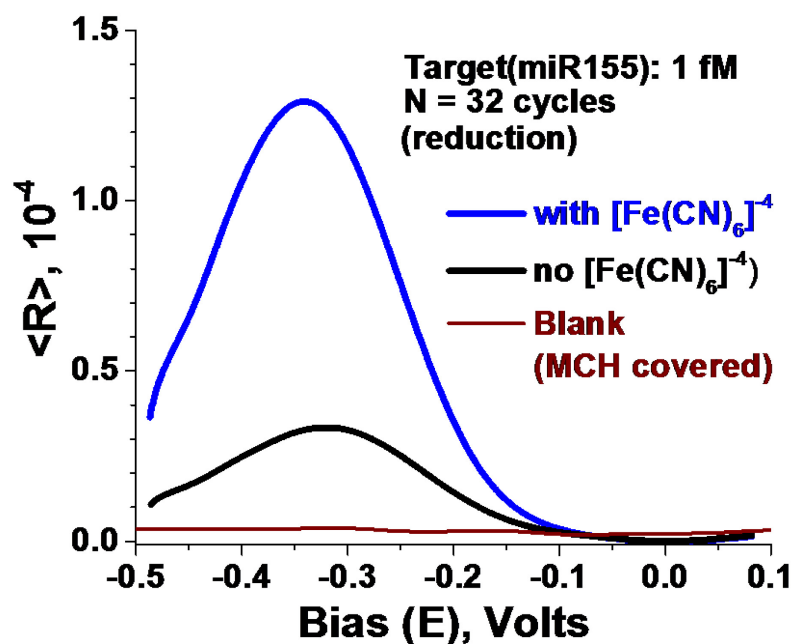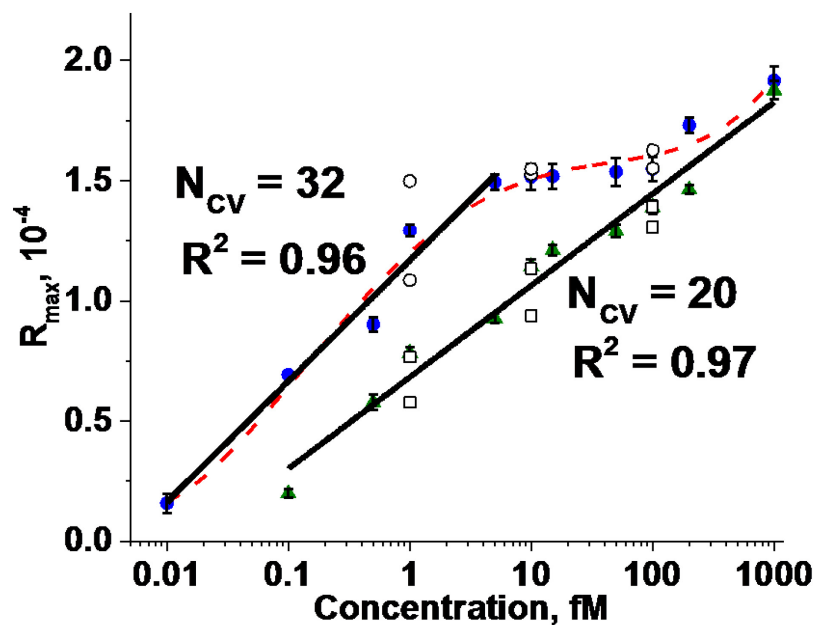**Figure S9:** Raw data showing peaks for MB^+/LMB redox

Figure S10: Typical oxidation (blue) and reduction (red) SEED-R signal on the control electrode for the three microwells (blank, P155, and P21) when the backfilling was not complete. All of the spots on each microwell showed a positive signal.
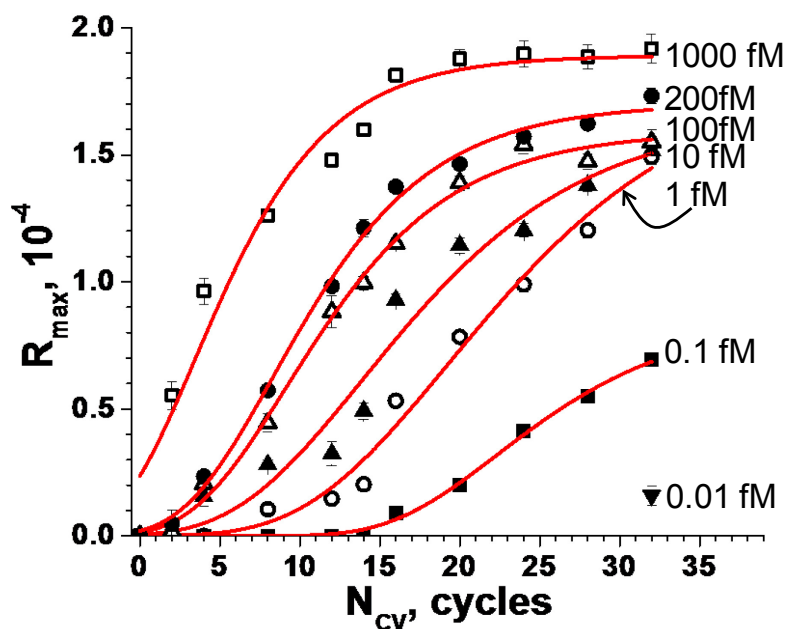
Figure S11: The SEED-R signal as a function of target concentration, [c]. The probe and target were P155 and miR-155, respectively. The fitness, $R^2 > 0.96$, indicated excellent correlation over a dynamic range of five orders of magnitude. The data was reproduced from our previous publication.[2]

Figure S12: Effect of including auxilary redox ion, $[Fe(CN)_6]^{4-}$ on EREB.

Figure S13: Effect of EREB cycles, N_{CV} on EREB for [c] ranging from 10^{-2} to 10^{3} fM
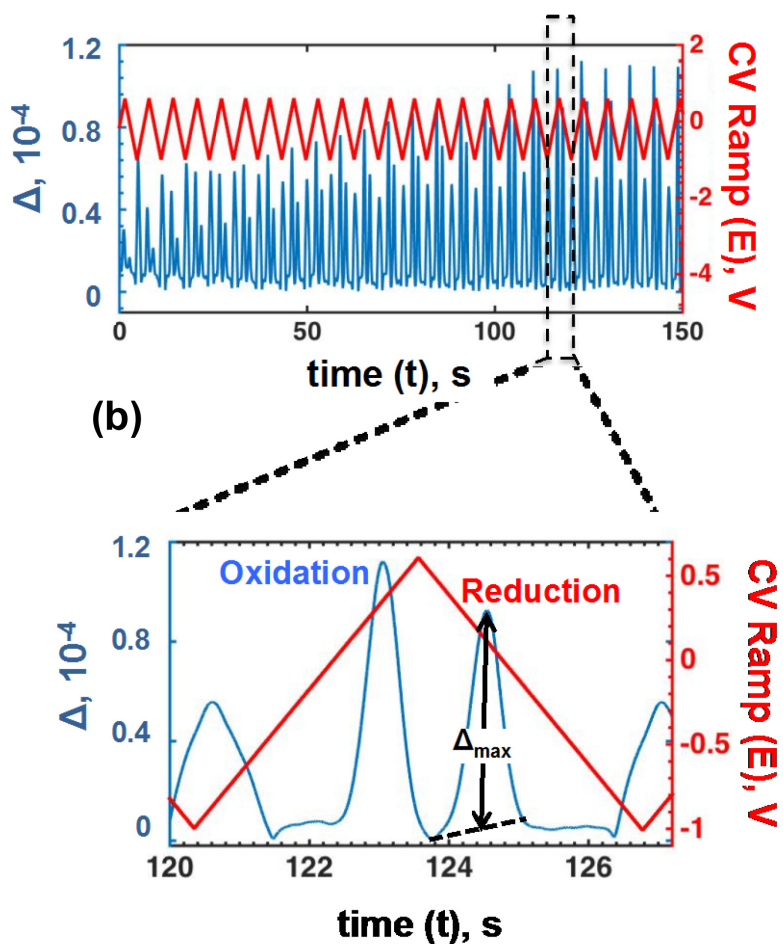
Figure S14: SEED-I raw data during MCH/ssDNA stripping showing the increase in $Fe(CN_6)^{3-/4-}$ redox peaks. The zoom-in panel shows one CV cycle with oxidation and a reduction signal peak of $Fe(CN_6)^{3-/4-}$.
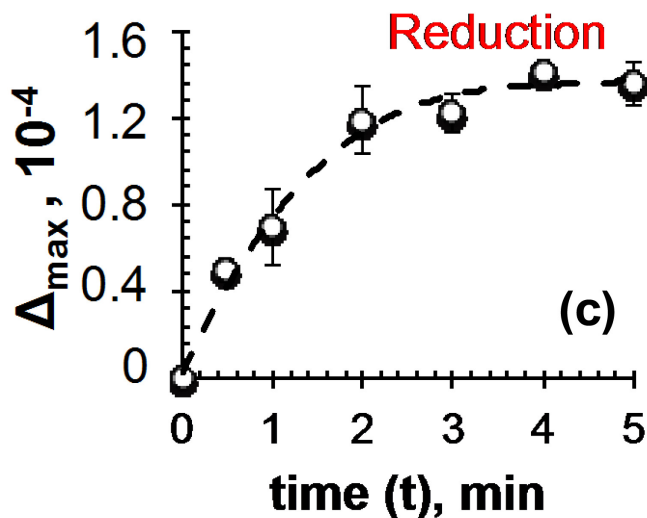
Figure S15: The Δ_{max} of $Fe(CN_6)^{3-/4-}$ redox during stripping.

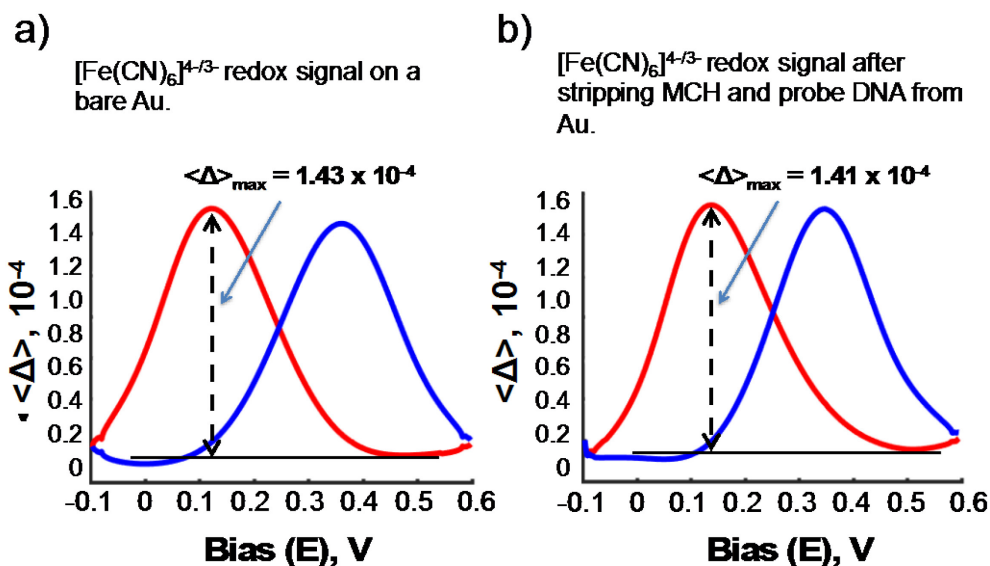**Figure S16:** Comparison of SEED-I redox signal for 50 mM $K_4[Fe(CN)_6]$ in 100 mM PB on (a) pristine Au after cleaning with piranha solution and (b) a Au electrode after the MCH was electrochemically removed. The nominally similar signal indicated that the removal of MCH after 5 min was complete.

S6. Fluorescence Analysis for Probe Coverage

The P155 probes tagged with Cy-3 fluorescent dye at 3' (Cy3-P155) were immobilized on the Au electrode of a chip. The electrode was a 0.08 cm x 0.8 cm rectangle patterned by lithography. A fluorescence emission spectrum was recorded at an excitation wavelength of 550 nm (F-4500 Fluorescence Spectrophotometer, Hitachi) (Figure S17(a)). The peaks were resolved by fitting three Gaussian curves at the

wavelengths noted in Table S1. The Gaussian peak at the wavelength of 551.7 nm corresponds to Au (Peak 1), 574.0 nm to Cy-3 (Peak 3), and 641.6 nm to P155 (Peak 2).

To avoid the quenching Cy3 dye, the gold surface was passivated with dielectric MCH. As shown in Figure S17(b), 1.51×10^{10} Cy3-P155 molecules/cm^2 showed a peak at 574.0 nm for Cy3 with negligible height (~0.01 a.u.), which improved by fourfold (0.42 a.u.) after MCH backfilling.

The deconvoluted Gaussian fluorescence curve, I_F, was obtained for films with a known amount of Cy3-tagged probe molecules deposited on a 6.4×10^2 cm^2 Au surface (Figure S17(c)).

A calibration curve was obtained by measuring peak of I_F as a function of known amount of molecules deposited on MCH passivated Au surface of same area (Figure S17(d)). From the fluorescence of immobilized probes (Figure S17(a)) and the calibration curve (Figure S17(d)), the probe coverage, N_P, was estimated to be $2.9 \pm 0.4 \times 10^{12}$ molecules/cm^2. The error was based on five chips. The coverage measured by fluorescence and qPCR was consistent, indicating that the coverage of probe ssDNA was uniform in the 50-µm microwell.
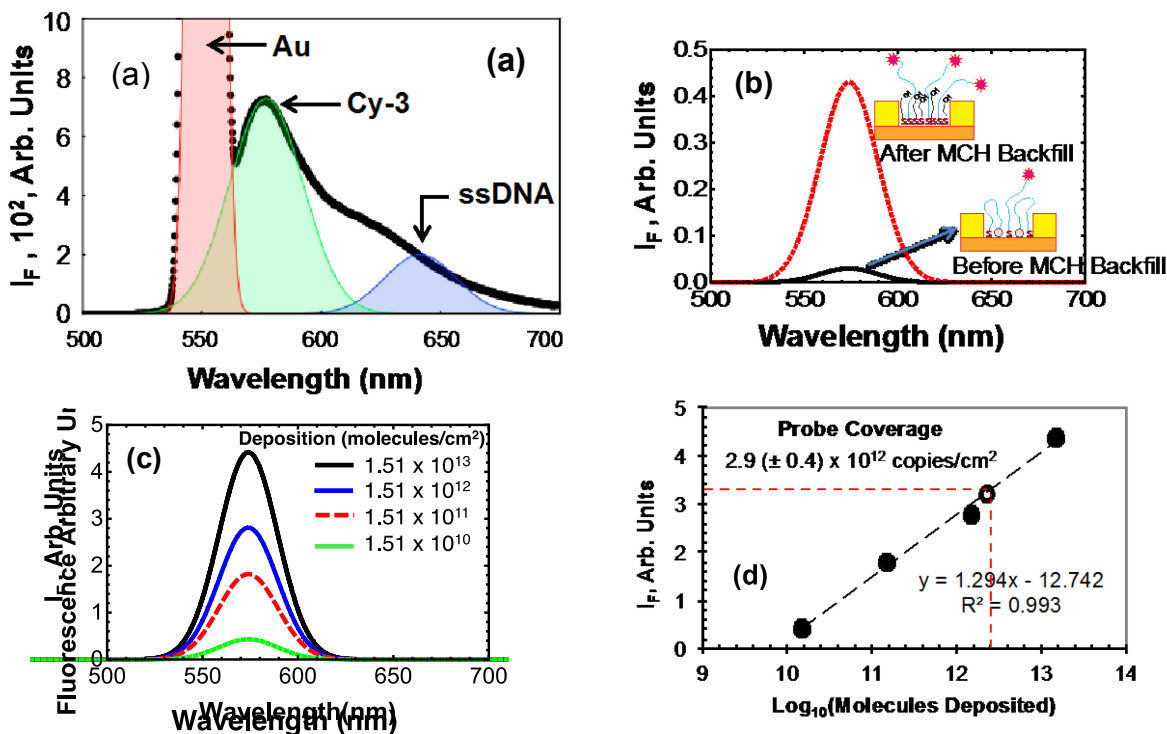

Figure S17: (a) Fluorescence emission spectrum of Cy-3-tagged ssDNA on a Au surface excited at 550 nm. (b) Gaussian peaks for the Cy3 fluorescence before and after MCH backfilling for 1.51×10^{10} Cy3-P155 / cm^2. (c) Fitted gaussian fluorescence peaks from different amounts of Cy-3-lbled ssDNA probe film. (d) Calibration curve showing linear fit of log$_{10}$(probe copy number, i.e., coverage) as a function of I_F.

Table S1. Gaussian parameters obtained from fitting the experimental data in Figure S17.

	Peak Number		
	1	2	3
K (nm)	4.4 ± 0.01	15.4 ± 0.11	15.0 ± 0.13
Lambda (nm)	551.7 ± 0.01	574.0 ± 0.04	641.6 ± 0.13

S7. Differential Pulse Voltammetry (DPV)

The chip was fabricated similar to that described in Section S1. The EREB was performed at N_{CV} = 5 cycles and target concentration of 1 pM. The electrode was subsequently backfilled. Among the two chips fabricated, the R_{max} for MB reduction on electrodes with good MCH backfill averaged at ~1.5×10^{-5} with no redox signal for $[Fe(CN)_6]^{4-/3}$. On the same chip, two electrodes with accidental defects at a few spots leading to poor backfill showed a twofold larger R_{max} and a redox signal for $[Fe(CN)_6]^{4-/3}$. A typical SEED signal for poor MCH backfill is shown in Figure S18.

To circumvent the overriding large capacitance current observed in CV, redox is measured by differential pulse voltammetry (DPV). DPV was performed using Autolab NOVA 2.1 on all of the electrodes with the following conditions: step = 0.005 V, modulation amplitude = 0.02 V, modulation time = 0.005 s; and interval time = 0.5 s. Consistent with the SEED results, the current due to MB reduction on a poorly backfilled electrode was significantly larger.

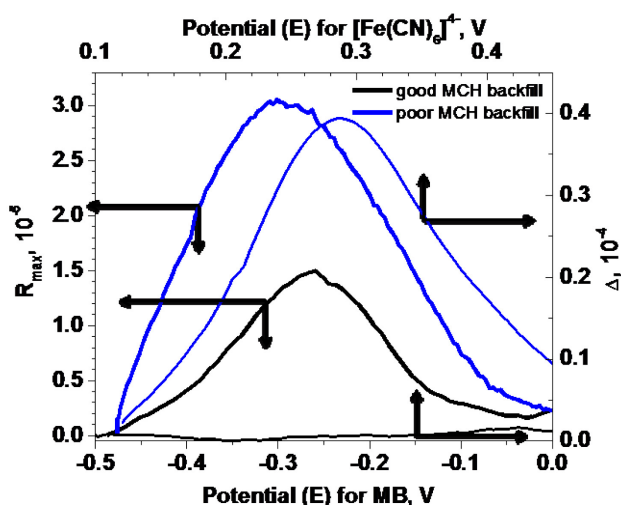The DPV for 10 µM MB and 50 mM $K_4[Fe(CN)_6]$ in 100 mM PB (pH 7.6) showed a strong peak due to MB reduction (Figure S19).

Figure S18: SEED signal comparing two spots on the same electrode with good and poor backfilling of MCH. Reduction of MB and $K_4[Fe(CN)_6]$ are shown for corresponding spots.
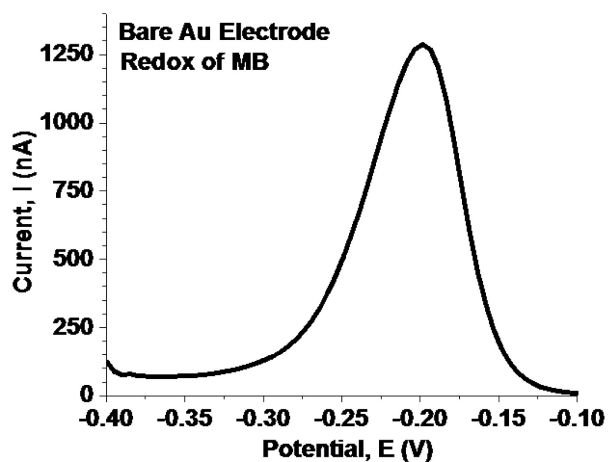
Figure S19: DPV showing the MB reduction on pristine Au electrode surface.

References

1. Yu, C. C.; Lee, S. W.; Ong, J.; Moore, D.; Saraf, R. F. Single Electron Transistor in Aqueous Media. *Adv. Mater.* **2013,** *25*, 3079-3084.

2. Raghunath, S.; Prasad, A.; Tevatia, R.; Gunther, J. R.; Roy, S.; Krishnan, S.; Saraf, R. F. Quantitative Electrochemical DNA Microarray on a Monolith Electrode with Ten Attomolar Sensitivity, 100% Specificity, and Zero Background. *Chemelectrochem* **2018,** *5*, 429-433.